Regional Retrieval Processor for Direct Broadcast High-Resolution Infrared Data

PAOLO ANTONELLI AND HENRY E. REVERCOMB

Space Science Engineering Center, University of Wisconsin–Madison, Madison, Wisconsin

GRAZIANO GIULIANI

Abdus Salam International Center for Theoretical Physics, Trieste, Italy

TIZIANA CHERUBINI, STEVEN BUSINGER, AND RYAN LYMAN

Mauna Kea Weater Center, Department of Meteorology, University of Hawai'i at Mānoa, Honolulu, Hawaii

STEPHEN TJEMKES AND ROLF STUHLMANN

EUMETSAT, Darmstadt, Germany

JEAN-LUC MONCET

Atmospheric Environmental Research, Inc., Boston, Massachusetts

(Manuscript received 27 April 2016, in final form 20 March 2017)

ABSTRACT

The Space Science Engineering Center, in collaboration with the Mauna Kea Weather Center at the University of Hawai'i at Mānoa, has developed a regional retrieval processor for high-spectral-resolution infrared data. The core of the processor makes use of an inversion system, referred to as Mirto, which combines, in a Bayesian way, the a priori knowledge of the atmospheric state, based on available numerical weather prediction forecasts, with the physical information embedded in satellite observations. Forecast temperature and water vapor mixing ratio fields over the central North Pacific Ocean are adjusted to produce synthetic radiances closer and closer to the *Suomi NPP* Cross-track Infrared Sounder (CrIS) observations taken in clear-sky conditions. The paucity of synoptic observations over this area and the highly homogeneous background represented by the ocean provide a good framework for the implementation of this hyperspectral data inversion system. Nearly real-time (less than 60 min from overpass time) Internet publication of retrieved atmospheric profiles is made possible by the availability of a direct broadcast system that provides data from the *Suomi NPP* platform (CrIS and VIIRS). The main goal for the implemented system is to provide the forecasting community with products suitable for nowcasting applications and for optimal data assimilation. The implemented processor has been running routinely since August 2013. Validation based on the comparisons of retrievals with rawinsonde data from Hilo, Hawaii, and Lihue, Hawaii, and GPS-derived total precipitable water from four stations, performed over a time period of more than 1 year, shows a statistically significant improvement on the background atmospheric state used as a priori information.

1. Introduction

Several polar-orbiting platforms (*Suomi NPP*, *MetOp-A* and *MetOp-B*, and *Aqua*) are currently flying high-spectral-resolution infrared instruments such as the Cross-track Infrared Sounder (CrIS) (Han et al. 2013), Infrared Atmospheric Sounding Interferometer (IASI) (Blumstein et al. 2004), and AIRS (Aumann et al. 2003). These instruments are capable of sensing the atmosphere to a finer vertical resolution than the traditional multichannel imagers such as VIIRS (Cao et al. 2014), AVHRR, MODIS (Cao et al. 2008), and so on. New missions are also planning to fly similar instruments: the European Meteosat Third Generation (MTG), which will be launching geostationary platforms carrying MTG InfraRed Sounder (IRS) (EUMETSAT 2014); European Organization for the Exploitation of Meteorological Satellites (EUMETSAT) Polar System Second

Corresponding author: Paolo Antonelli, paoloa@ssec.wisc.edu

DOI: 10.1175/JAMC-D-16-0144.1

Generation (EPS-SG), which will fly IASI of New Generation (IASI-NG) (Crevoisier et al. 2014); or the Climate Absolute Radiance and Refractivity Observatory (CLARREO) mission (Cooke et al. 2014), which is aiming to use high-spectral-resolution infrared data for climatological applications. These sensors are expected to play an increasingly important role in refining the characterization of the atmospheric state at higher temporal and vertical resolutions.

Since AIRS data (Aumann et al. 2003) became available in 2001, high-spectral-resolution satellite infrared data have been used by the modeling community mostly in the form of calibrated spectral radiances. The choice of using radiances (level 1 data) has been driven by the need for consistent assimilation of different satellite observations, which led operational meteorological centers to assimilate them directly using variational data assimilation systems. However, more recently, with the increased number of hyperspectral infrared sensors in polar orbits and the prospect of a future geostationary instrument, there has been a renewed interest in assimilating the thermodynamic fields obtained from radiances (generally referred to as retrievals or level 2 data), especially for limited area models (Chou et al. 2009, 2010; Jones and Stensrud 2012; Reale et al. 2008; Singh et al. 2012). Level 2 data can be obtained from level 1 data via inversion (retrieval) algorithms by means of either an optimal estimation (Rodgers 2000) or a statistical approach (Smith et al. 2012).

This paper presents a regional processor for high-spectral-resolution infrared data based on Mirto (not an acronym), an optimal estimation retrieval system. The processor has been implemented at the Mauna Kea Weather Center (MKWC), a weather research and forecast facility funded by the astronomical observatories on Mauna Kea (Businger et al. 2002; Cherubini et al. 2011). The system generates products in the forms of soundings, instability maps of convective available potential energy (CAPE), total precipitable water (TPW), lifted index (LI), and scaled projected states (SPS; or transformed soundings), optimally designed for NWP data assimilation purposes (Migliorini et al. 2008; Migliorini 2012). The term ''optimally'' is used after Migliorini's demonstration of the equivalence, under specific conditions, between the radiance and retrieval assimilations. When these conditions (described in section 2b) are met, not only is the assimilation of retrievals equivalent to radiance assimilation, but it also bears the following advantages: it requires smaller computational loads, and it does not require any knowledge regarding the sensor characteristics (spectral resolution, instrument noise, apodization, etc.). Both these peculiarities make the use of transformed retrievals particularly attractive to small forecasting centers. Therefore, the system was designed to provide quasi-real-time (less than 60 min from overpass time) vertical profiles of temperature and water vapor mixing ratio (level 2 products), their related instability indices [level 3 (L3) products], and the Migliorini transformed retrievals for the north-central Pacific Ocean area centered on the Hawaiian archipelago. The products generated are currently archived and will be distributed to users in netCDF format after the system has been presented in a peer-reviewed publication. The implementation of the regional service was made possible by the availability of a direct broadcast system, operated by the Space Science Engineering Center (SSEC) of the University of Wisconsin–Madison in collaboration with the National Weather Service and the University of Hawai'i at Mānoa, which provides quasi-real-time level 1 CrIS data (within 15 min from overpass), and by the MKWC operational run of the Weather and Research Forecast (WRF) Model system (Klemp et al. 2007) (http://www.wrf-model.org), which provides hourly forecasts over the central Pacific domain (Fig. 1). The core of the processor, Mirto, combines the a priori information derived from the MKWC model fields with the physical information embedded in the satellite observations according to a Bayesian paradigm. The system has been operating daily since August 2013. Validation of retrieved fields has been performed over more than one year to assess their accuracy.

The relevance of the processor presented in this paper is to be found in the use of direct broadcast data to generate retrieved atmospheric fields for short-term forecasting and optimal data assimilation purposes. On one hand, in fact, the retrieved profiles allow for a characterization of the stability of the atmosphere over the domain of interest, which is useful in nowcasting applications. On the other hand, the application of the Migliorini's transformation to the derived soundings would allow the local assimilation systems to generate a custom analysis within one hour from the satellite overpass. The MKWC is directly involved in an international effort, supported by the EUMETSAT, aimed to develop a pseudo-operational Rapid Update Cycle forecast system based on the assimilation of the SPS (transformed retrievals) from IASI and CrIS. Provided that the retrieval meets the accuracy needed for a positive impact on data assimilation, and the timeliness of the atmospheric products is reduced to 30 min from overpass time, the implementation of the processor would become an important element in the future development of the MKWC forecasting and nowcasting capabilities.

The paper is structured as follows: section 2 provides a theoretical background for the inversion core Mirto, the implementation of the regional processor system is

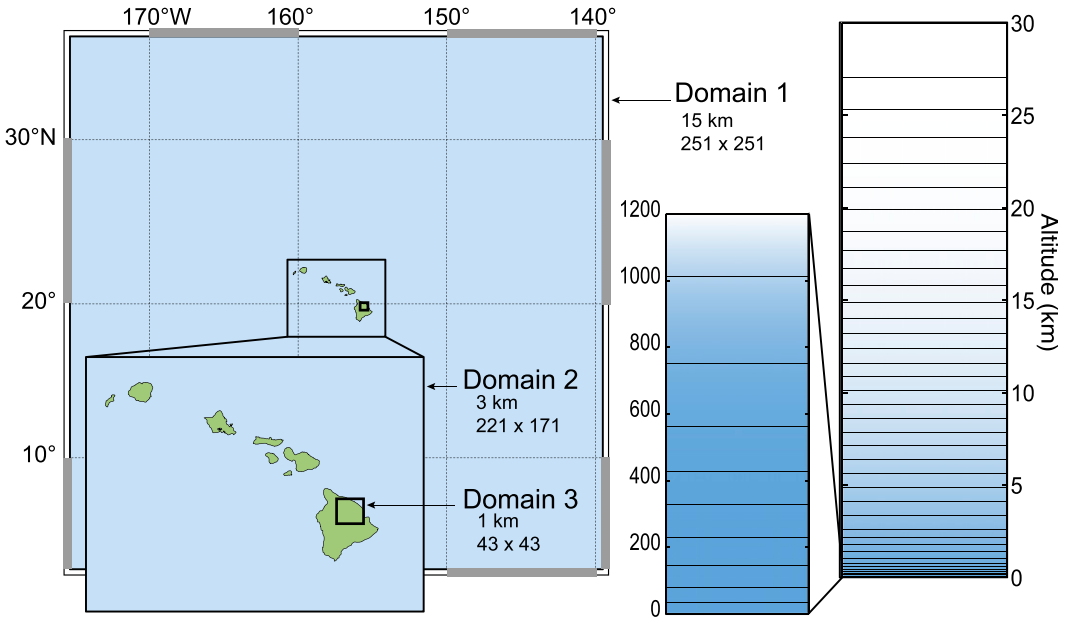

FIG. 1. Domain of the WRF system operated at the MKWC, which provides hourly forecasts over the central Pacific area.

described in detail in section 3, validation strategies and results are presented in section 4, section 5 describes the retrieval diagnostics in terms of spectral residuals, and conclusions and future works are presented in section 6.

2. Mirto

Mirto is an inversion system based on optimal estimation, implemented in Python, and designed to run on multicore computers. It is an evolution of the Matlab-based University of Wisconsin Physical Retrieval (UWPHYSRET) package, (Antonelli et al. 2008), developed at SSEC, with the same physics but fully recoded in Python and improved in efficiency (currently, the system inverts one CrIS observation in less than 0.5 s using six cores). Mirto allows for the retrieval of atmospheric variables from level 1 (calibrated radiances) data observed by high-spectral-resolution infrared instruments. These variables include atmospheric temperature, water vapor mixing ratio, carbon dioxide, ozone, and surface temperature and emissivity. In addition, Mirto generates the Migliorini transformed retrievals, or SPS, for temperature and water vapor along with maps of instability indices (CAPE, LI, and TPW). Mapping of observable (radiances) into non-observable variables in Mirto is achieved through Bayesian inversion (Rodgers 2000) and, at this stage, is formulated for clear-sky conditions only. Mirto uses the Atmospheric and Environmental Research (AER) optimal spectral sampling (OSS) clear-sky radiative transfer model (plane-parallel geometry) for the computation of simulated radiances and analytical Jacobians based on localized training (Moncet et al. 2008). The AER OSS was chosen for its good balance between speed and accuracy that makes the model suitable for applications like Mirto, the computational core of the described regional service. The Mirto system is intended to be open source and currently works with CrIS and IASI observations. Mirto's modular nature allows for its application to other current and future high-spectral-resolution instruments such as MTG IRS, and AIRS. Mirto, and its precursor UWPHYSRET, have been adopted by EUMETSAT as the foundation for the algorithm theoretical basis document of MTG IRS (EUMETSAT 2014) and for the development of the level 2 validation of demonstration processor in the framework of MTG IRS–related activities.

a. *Theoretical background*

The inversion in Mirto is based on the minimization of the cost function $J(\mathbf{x})$ defined as

$$J(\mathbf{x}) = (\mathbf{x} - \mathbf{x}^b)^{\mathrm{T}}\mathbf{B}^{-1}(\mathbf{x} - \mathbf{x}^b) + [\mathbf{y}_{\mathrm{rad}} - H(\mathbf{x})]^{\mathrm{T}}\mathbf{R}_{\mathrm{rad}}^{-1}[\mathbf{y}_{\mathrm{rad}} - H(\mathbf{x})]. \quad (1)$$

The first term on the right-hand side of Eq. (1) can be thought as the volume in the state space, where the solution is likely to be found with a certain confidence before the observation is made, and it is given by the square difference of the retrieved state $\mathbf{x}$ to the a priori or

background state $\mathbf{x}^b$ weighted by the a priori covariance matrix $\mathbf{B}$. The second term on the right-hand side of Eq. (1) represents the region in which the states consistent with the observations could be found, and it is given by the distance between the measurements $\mathbf{y}_{\text{rad}}$ and the retrieved state mapped into measurement space using the observation operator H and weighted by the total error covariance matrix, $\mathbf{R}_{\text{rad}}$, defined as

$$\mathbf{R}_{\text{rad}} = \mathbf{R}_m + \mathbf{R}_H, \tag{2}$$

where $\mathbf{R}_m$ represents the errors in the measurements (instrument noise), and $\mathbf{R}_H$ represents the errors in the observation operator (forward model).

In particular, the observation operator error covariance matrix $\mathbf{R}_H$ represents the errors associated with the radiative transfer model like the errors in the spectroscopic parameters (line position and half-width) and the errors due to the atmospheric–surface variables not specifically accounted for in the radiative transfer calculations. This component of the total error covariance matrix is difficult to estimate, and it is not clear how an erroneous characterization would influence the retrieval accuracy. The estimation of $\mathbf{R}_{\text{rad}}$ is described in section 2.

The minimization of the cost function $J(\mathbf{x})$ [Eq. (1)] is done using the Marquardt–Levenberg (ML) iterative scheme (Levenberg 1944; Marquardt 1963), whose ith iteration is given by

$$\mathbf{x}^{i+1} = \mathbf{x}^i + [(1+\gamma_i)\mathbf{B}^{-1} + (\mathbf{H}^i)^{\mathrm{T}}\mathbf{R}_{\text{rad}}^{-1}\mathbf{H}^i]^{-1} \times \{(\mathbf{H}^i)^{\mathrm{T}}\mathbf{R}_{\text{rad}}^{-1}[\mathbf{y}_{\text{rad}} - H(\mathbf{x}^i)] - \mathbf{B}^{-1}(\mathbf{x}^i - \mathbf{x}^b)\}, \tag{3}$$

where $\mathbf{H}^i = \partial H/\partial \mathbf{x}^i$ is the Jacobian of the observation operator, and the ML parameter γ_i is changed from one iteration to the next one to provide a mixed approach between the steepest descend approach (Avriel 2003), where $\gamma \to \infty$ and the Gauss–Newton approach (Nocedal and Wright 1999), where $\gamma \to 0$, that is preferred near the solution because then the convergence is quadratic. The strategy for selecting γ is relatively arbitrary. In principle, γ should be chosen depending on the degree of linearity of the observation operator. At this stage, in the implemented system, γ is chosen according to the degree of increase or decrease of χ^2, defined by Eq. (5.25) of Rodgers (2000) as

$$\chi^2 = [\mathbf{y} - H(\mathbf{x})]^{\mathrm{T}}\mathbf{R}_{\text{rad}}^{-1}[\mathbf{y} - H(\mathbf{x})]. \tag{4}$$

At the first iteration, γ_0 is set to 3. As the iterative process goes on, the value of γ is modified according to the change of the cost function between one iteration and the previous one. If χ^2 increases, γ is multiplied by a factor of 5; if χ^2 decreases, γ is divided by a factor of 2. When convergence criterion is met, γ is set to 0, and one last iteration is performed to calculate the final solution $\hat{\mathbf{x}}$. It is worth mentioning that the χ^2 is calculated only over the selected channels (shown by the green dots in Figs. 19 and 20, described in more detail below).

The convergence criterion is met when the change in the state space, normalized by the state uncertainty d_i^2 is smaller than a defined threshold $\Xi_{\text{convergence}}$. Following Rodgers' notation (Rodgers 2000),

$$d_i^2 = (\mathbf{x}_i - \mathbf{x}_{i+1})^{\mathrm{T}}\mathbf{S}^{-1}(\mathbf{x}_i - \mathbf{x}_{i+1}), \tag{5}$$

where, according to Eq. (5.30) of Rodgers (2000),

$$\mathbf{S}^i = [(1+\gamma_i)\mathbf{B}^{-1} + (\mathbf{H}^i)^{\mathrm{T}}\mathbf{R}_{\text{rad}}^{-1}\mathbf{H}^i]^{-1}; \tag{6}$$

then, if

$$\frac{d_i^2}{n} < \Xi_{\text{convergence}} \ll 1, \tag{7}$$

where n is the number of elements of the state vector, the minimization process has reached convergence. The threshold value is chosen arbitrarily. Good results have been achieved with a value of $\Xi = 0.03$. When convergence is not met, the iterative process stops after a maximum number of 10 iterations, and a flag indicating that convergence has not been reached is raised.

The knowledge of the atmospheric state prior the observations, generally called a priori or *background* knowledge, plays an important role in the retrieval algorithm. This a priori consists of two parts: the best estimate of the atmospheric state prior the observation is taken, $\mathbf{x}^b$ and an associated covariance matrix $\mathbf{B}$ representing the error–likelihood of the estimate.

In Mirto, the a priori $\mathbf{x}^b$ is also used to characterize the *first guess* $\mathbf{x}_0$ and the linearization point $\mathbf{x}_a$ in Eq. (3). In the current implementation, the a priori $\mathbf{x}^b$ is derived using NWP model short-term forecast validating the time of the satellite overpass for atmospheric temperature and water vapor. Atmospheric ozone and carbon dioxide a priori are derived from climatological datasets (http://www.esrl.noaa.gov/gmd/dv/iadv/graph.php?code=HIH&program=ozwv&type=vp and http://www.esrl.noaa.gov/gmd/ccgg/trends/, respectively).

Specifically, the atmospheric temperature and water vapor are provided by the MKWC, which runs the WRF Model operationally over the north-central Pacific area. The model configuration, at the time of this study, encompasses three two-way nested domains, with horizontal resolution spacing of 15, 3, and 1 km (Fig. 1);

40 levels in the vertical are used. The vertical spacing is on the order of tens of meters for the levels nearest the ground and gradually increases with height. The model top is fixed at 10 hPa, which corresponds to a height of about ~25 km above the ground level. The WRF Model is run twice daily with 0000 and 1200 UTC initial conditions produced by a WRF data assimilation system (Barker et al. 2012). Boundary conditions are updated every 6 h using model output from the National Centers for Environmental Prediction (NCEP) Global Forecast System (GFS). Each forecast cycle produces a 60-h-long forecast as output. More on the MKWC WRF configuration can be found in Cherubini et al. (2006, 2011).

Mirto uses WRF output from the 15-km horizontal grid domain from the most current WRF forecast cycle available, which is the same order of magnitude as the CrIS's field of view (FOV). Because the *Suomi NPP* overpass times over the central Pacific area are close to 0000 and 1200 UTC, the most current WRF forecast validating the satellite overpass' time is usually the WRF forecast initialized 12 h earlier. Since the WRF Model forecast extends only up to 10 hPa, climatological profiles available within the AER Line-By-Line Radiative Transfer Model (LBLRTM) libraries are used to extrapolate the a priori for temperature and water vapor up to satellite altitude at 0.1 hPa.

The a priori for surface temperature (ST) is obtained as random perturbation of the lowest level a priori atmospheric temperature using a Gaussian probability distribution with mean equal to 0 K and standard deviation of 3 K, while the surface emissivity (SE) is represented in the form of principal component amplitudes. Different sets of principal components are generated and used for each surface type according to the classification scheme defined by the International Geosphere–Biosphere Programme (IGBP) (Loveland et al. 1991, 1999). For observations over the ocean, one set of PCs is generated using simulated Masuda emissivities (Masuda et al. 1988) stratified by different viewing angles (between 0° and 60°) and wind speeds (between 0 and 30 m s^{-1}). For observations over land, dedicated sets of PCs are calculated for each IGBP class by using for training all the emissivity contained in the National Aeronautics and Space Administration (NASA) SE atlas retrieved from IASI global observations over the last six years (Zhou et al. 2011). For each IGBP class, the principal components are calculated after applying the logit transformation to the original emissivity spectra:

$$z(\nu_i) = \log\left[\frac{\varepsilon(\nu_i)}{1-\varepsilon(\nu_i)}\right]. \tag{8}$$

Examples of the logit-transformed emissivity derived for the NASA IASI emissivity atlas for IGBP classes 1 (evergreen needleleaf forests) and 10 (grasslands) along with the logit-transformed ocean emissivity from the Masuda model are shown in Fig. 2.

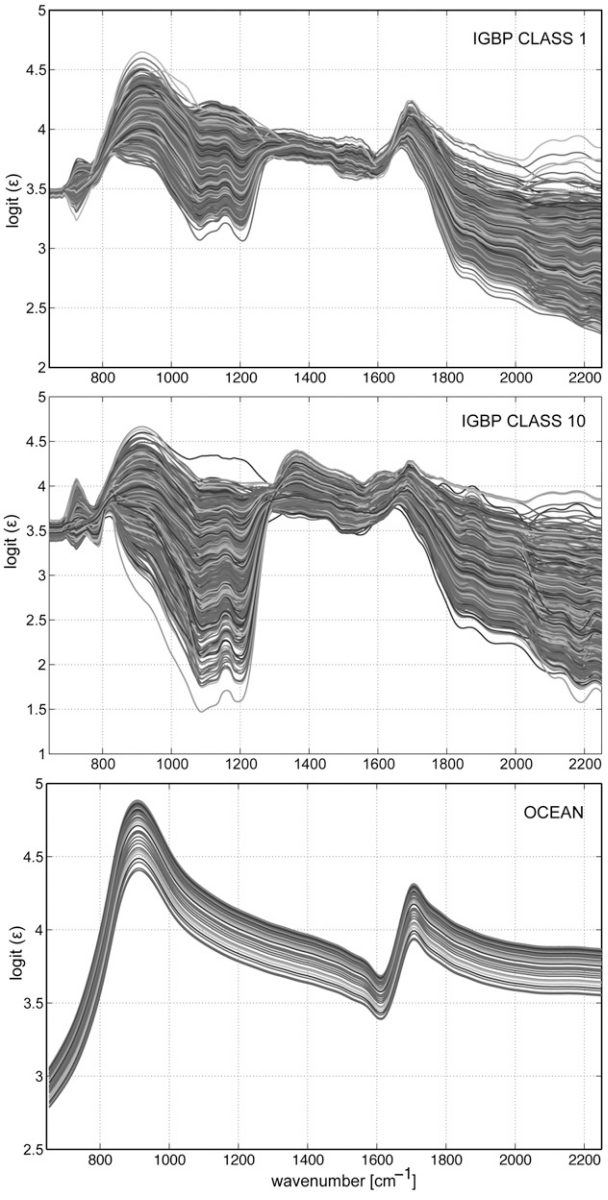

FIG. 2. Logit of surface emissivities for IGBP classes 1 and 10, and for ocean.

Using the correct IGBP class, a small number (3–7) of principal component amplitudes are then used to represent the full SE spectrum to be associated to each CrIS observation. The a priori is then obtained by setting all the amplitudes to 0, which implies that the best estimate of SE, before the observation is made, corresponds to the mean of the training set used for that specific class. Instead, the a priori covariance is

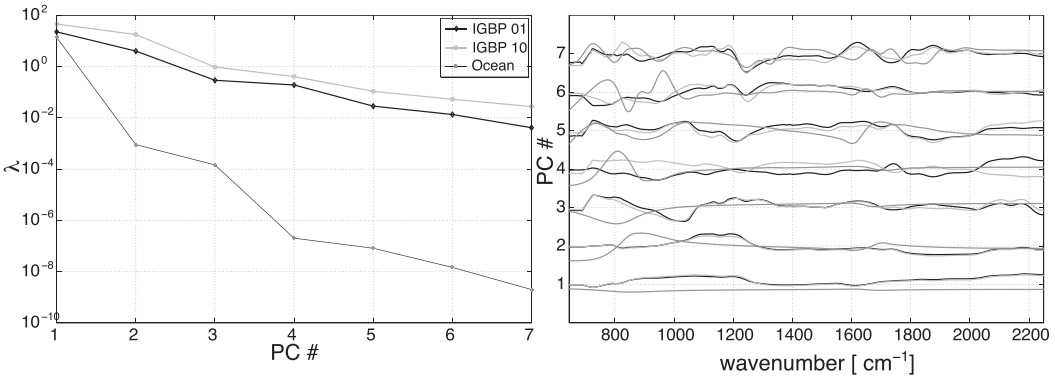

FIG. 3. First seven (left) eigenvalues and (right) PCs derived for land (IGBP classes 1 and 10) and ocean emissivities in logit space.

provided by the 3–7 leading eigenvalues for the selected class. Figure 3 compares the first 7 eigenvalues and eigenvectors of the logit-SE covariance matrix (principal component amplitudes) for the same classes shown in Fig. 2.

It is worth remarking that, in principle, the choice of the first guess (here equal to the a priori) should only affect the efficiency (convergence speed) and not the accuracy of the retrieval process. However, the shape of the cost function can be relatively complex with local maxima and minima. Therefore, it cannot be excluded that the accuracy of the result of the iterative approach will depend also on the first guess.

1) BACKGROUND COVARIANCE MATRIX

The background covariance error represents the uncertainty associated to the a priori state $\mathbf{x}^b$. The complete background covariance used by Mirto is a block matrix composed of five blocks:

- the atmospheric components derived from the forecast model: T and $\log(q)$ [where q is the specific humidity (kg kg^{-1})],
- the atmospheric components for CO_2: a diagonal matrix with constant values of 16 ppmv^2 on the diagonal,
- the atmospheric components for O_3: a climatological matrix of $\log(w)$ [where w is the ozone mixing ratio (kg kg^{-1})] derived from ozonesondes,
- the surface component for ST: single value set to 3 K, and
- the surface component for the SE amplitudes: the diagonal matrix with the eigenvalues of the corresponding SE IGBP class (as shown in Fig. 3) in LOGIT space.

For atmospheric temperature and water vapor, in the current implementation, the a priori or background covariance has been estimated following the National Meteorological Center (NMC) method (Parrish and Derber 1992). At first, the model perturbations are calculated and used as a proxy for the estimate of the forecast error. For the NMC method, in fact, the model perturbations, for regional applications, can be calculated as the differences between the WRF 24-h forecasts and the 12-h forecasts valid at the same time. Climatological estimates of the background error may then be obtained by averaging these forecast differences over a period of time (usually a month). The 40 consecutive days spanning the time frame June through July 2013 were used to calculate the background covariance (BE) matrix currently in use, and both the 0000 and 1200 UTC cycles output were included in the statistics. As it would be desirable to use a dataset representative of a larger number of cases/events through the meteorological year, the covariance matrix will be refined in the future. The uppermost model level is located at 10 hPa; therefore, the covariance for temperature above 10 hPa had to be arbitrarily calculated starting from the highest WRF level temperature covariance and adding to it a constant increment (5%–10%) at each level from 10 hPa to the top of the atmosphere, at 0.1 hPa. The covariances for water vapor above 10 hPa are set to the same value of the uppermost WRF level water vapor covariance. Figure 4 shows the full background covariance blocks for T–Q and O_3, respectively.

The background covariance for ozone is set to climatological values obtained from in situ observations of ozonesondes (http://www.esrl.noaa.gov/gmd/dv/ftpdata.html). For the carbon dioxide, the variances have been set arbitrarily to 16 ppmv^2. In the same way, the ST variance has been set to 3 K^2, while for the SE amplitudes, the variances are set to the eigenvalues derived for the characteristics (IGBP class) of the observations (as shown in Fig. 3).

Since Mirto retrieves temperature, water vapor, ozone, ST, and SE simultaneously, the role of the cross-correlation terms in the a priori covariance are

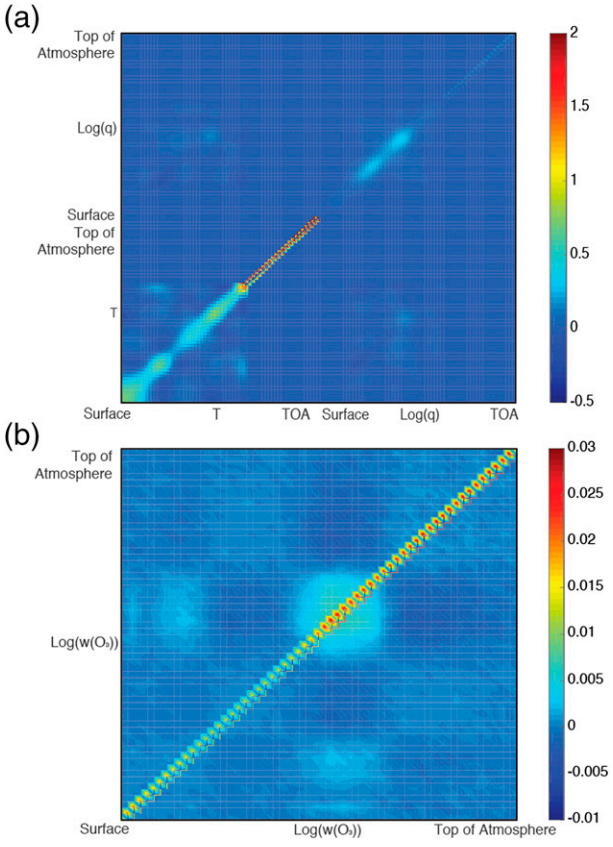

FIG. 4. (a) Background (a priori) covariance matrix for temperature and water vapor. The matrix is derived from a dataset of differences between the MKWC WRF 24-h forecasts and the 12-h forecasts verifying at the same time and contains cross-correlation terms between the two variables. (b) Background (a priori) covariance matrix for ozone. The matrix is derived from climatological values $\log[w(O_3)]$ from ozonesondes [where $w(O_3)$ is the ozone mixing ratio ($\mathrm{kg\,kg^{-1}}$)].

important. At this stage, only the cross-correlation terms between temperature and water vapor mixing ratio are taken into account, while every other cross-correlation term is set to 0 to reflect the lack of information on the interdependencies among the other variables.

The estimation of the background covariance matrix prepared as described above is not fully mature/complete yet. Other methodologies to calculate the background covariance error for the WRF temperature and water vapor will be investigated. The goodness/accuracy of the retrieval algorithm is strongly dependent on the background covariance matrix. In fact, if the error covariance information provided by the a priori is such that the satellite observations are not constrained enough, the posterior error covariance of the retrievals of the atmospheric state could be worse than the a priori error covariance, a situation that clearly needs to be avoided. On the other hand, if the a priori knowledge is too constraining, only part of the information embedded in the satellite observations could be exploited. This situation should be avoided as well.

2) TOTAL ERROR COVARIANCE MATRIX

The total error covariance matrix $\mathbf{R}_{\mathrm{rad}}$ as defined in Eq. (2) has two components, which were estimated from retrieval residuals,

$$\boldsymbol{\rho}_{\mathrm{rad}} = \mathbf{y}_{\mathrm{rad}} - H(\hat{\mathbf{x}}_{\mathrm{ret}}), \tag{9}$$

obtained from a large dataset of clear-sky retrievals that reached convergence. The first term on the right side of Eq. (2) $\mathbf{R}_m$, associated to the instrument noise, was obtained from the covariance of the spectral residuals, $\mathbf{R}_m = \mathrm{cov}(\boldsymbol{\rho}_{\mathrm{rad}})$, while the second term on the right side of Eq. (2), $\mathbf{R}_H$, associated to the systematic error because of the forward model uncertainties, was estimated using the mean of the spectral residuals, $\mathbf{R}_H = E(\boldsymbol{\rho}_{\mathrm{rad}})E(\boldsymbol{\rho}_{\mathrm{rad}})^{\mathrm{T}}$.

Figure 5 compares the square root of the diagonal elements of the total error covariance, $\mathbf{R}_{\mathrm{rad}}$, used by Mirto with the CrIS nominal noise (solid dark line) for all the channels used in the inversion process. [Figures 19 and 20, described in more detail below, show the individual components of $\mathbf{R}_{\mathrm{rad}}$ by presenting the square roots of the diagonal elements of $\mathbf{R}_m$ (red lines labeled as σ) and $\mathbf{R}_H$ (blue lines labeled as μ) superimposed on the CrIS nominal noise (black dashed lines) for the longwave (LW) and midwave (MW) portion of the spectrum.] The proper characterization of $\mathbf{R}_H$ is still an area of active research.

b. *Scaled projected states*

The determination of the atmospheric state (retrievals) from passive high-spectral-resolution infrared radiances is an ill-posed problem, and the solution $\hat{\mathbf{x}}$ provided by Eq. (3) is obtained by adding prior constraints to complement the instrument measurements. The dependence of the retrievals from the prior information makes their assimilation in NWP models not optimal unless the inversion and assimilation systems share the same a priori. This led, in the past, to the development of direct radiance assimilation schemes. Migliorini (2012) demonstrated that satellite observations in SPS form, obtained by a specific transformation of the retrievals, represent, under well-defined circumstances, a valid (equivalent) alternative to the assimilation of radiances. The circumstances are that 1) the forward model H is approximately linear in proximity of $\hat{\mathbf{x}}$ within a region of radius comparable to the retrieval error, and 2) the a priori matrix used in the inversion has larger variance than the one used in the assimilation (Migliorini et al. 2008; Migliorini 2012;

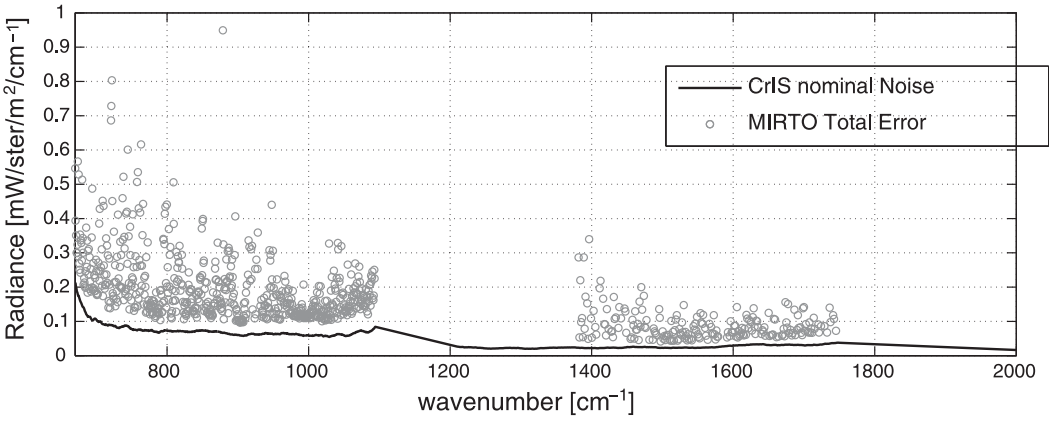

FIG. 5. Square root of the diagonal elements of the total error covariance matrix $\mathbf{R}_{\text{rad}}$ (gray circles) compared with the CrIS nominal noise (black line) for all channels used in the retrieval process.

Prates et al. 2016). When these circumstances are verified, the assimilation of satellite observations can be performed using the SPS without the need of a nonlinear radiative transfer model as observation operator. Following Migliorini (2012), Mirto generates the SPS, at first, by transforming the retrievals $\hat{\mathbf{x}}$ into

$$\mathbf{y}_{\text{ret}} \equiv \hat{\mathbf{x}} - \mathbf{x}^b + \mathbf{K}\mathbf{H}'\mathbf{x}^b, \tag{10}$$

where $\mathbf{H}' = \mathbf{\Sigma}_p^{-1} \times \mathbf{L}_p^{\mathrm{T}} \times \mathbf{H}$ is the Jacobian normalized using the p nonsingular eigenvectors $\mathbf{L}_p$ associated to the largest eigenvalues $\mathbf{\Sigma}_p^2$ of total error covariance $\mathbf{R}_{\text{rad}}$ such that $\mathbf{R}_{\text{rad}} \simeq \mathbf{L}_p\mathbf{\Sigma}_p^2\mathbf{L}_p^{\mathrm{T}}$, and $\mathbf{K}$ is the Kalman gain given by

$$\mathbf{K} = \mathbf{B}\mathbf{H}'^{\mathrm{T}}(\mathbf{H}'\mathbf{B}\mathbf{H}'^{\mathrm{T}} + \mathbf{I}_p)^{-1}, \tag{11}$$

where $\mathbf{I}_p$ is the identity matrix in the p-dimensional space spanned by the columns of $\mathbf{L}_p$.

To obtain the SPS $\mathbf{y}'_{\text{ret}}$, Eq. (23) of Migliorini (2012), the scaled components of the $\mathbf{B}^{1/2}\mathbf{y}_{\text{ret}}$ are projected onto the direction of the columns of $\mathbf{V}_r$, that is, the r nonsingular eigenvectors of the signal-to-noise matrix, $\mathbf{S} = \mathbf{H}'_{\text{ret}}\mathbf{B}^{1/2}$, with eigenvalues larger than one, derived from the decomposition $\mathbf{S} \simeq \mathbf{U}_r\mathbf{\Lambda}_r\mathbf{V}_r^{\mathrm{T}}$ (where $\mathbf{U}_r$ and $\mathbf{V}_r$ are respectively the r left and right eigenvectors of $\mathbf{S}$ associated to the $\mathbf{\Lambda}_r$ eigenvalues larger than 1):

$$\mathbf{y}'_{\text{ret}} = \mathbf{\Lambda}_r^{-1}(\mathbf{\Lambda}_r^2 + \mathbf{I}_r)\mathbf{V}_r^{\mathrm{T}}\mathbf{B}^{-1/2}\mathbf{y}_{\text{ret}}, \tag{12}$$

where $\mathbf{I}_r$ is the identity matrix in the r-dimensional space spanned by $\mathbf{V}_r$. The observation operator, Eq. (24) of Migliorini (2012), associated to $\mathbf{y}'_{\text{ret}}$ is then

$$\mathbf{H}'_{\text{ret}} = \mathbf{\Lambda}_r\mathbf{V}_r^{\mathrm{T}}\mathbf{B}^{-1/2}, \tag{13}$$

where $\mathbf{\Lambda}_r$ are the r eigenvalues of $\mathbf{S}$ larger than 1. Figure 6 shows the temperature and water vapor components of the assimilation operator.

Using the SPS, the assimilation problem becomes, using Eqs. (35) and (36) of Migliorini (2012),

$$\hat{\mathbf{x}}^{\text{ret}*}_{\text{MAP}} = \mathbf{x}^{b*} + \mathbf{K}^{\star}_{\text{ret}}(\mathbf{y}'_{\text{ret}} - \mathbf{H}'_{\text{ret}}\mathbf{x}^{b*}), \tag{14}$$

where

$$\mathbf{K}^{\star}_{\text{ret}} = \mathbf{B}^*\tilde{\mathbf{H}}'^{\mathrm{T}}_{\text{ret}}(\tilde{\mathbf{H}}'_{\text{ret}}\mathbf{B}^*\tilde{\mathbf{H}}'^{\mathrm{T}}_{\text{ret}} + \mathbf{I}_r)^{-1}, \tag{15}$$

$\mathbf{B}^*$ being the background assimilation covariance and $\mathbf{x}^{b*}$ the assimilation background. The SPS currently generated by Mirto contains 61 levels of temperature in (K) and 61 levels of $\ln(q)$ in (kg kg^{-1}), with the first level being temperature near the surface, the 61st element being temperature at the top of the atmosphere, the 62nd element being $\ln(q)$ at the surface, and the 122nd element being $\ln(q)$ at the top of the atmosphere to be consistent with $\mathbf{H}'_{\text{ret}}$. Also, $\mathbf{B}^*$ is expected to be consistent with the order and the units of $\mathbf{B}$ and $\mathbf{x}$, which means that $\tilde{\mathbf{H}}'_{\text{ret}} = \mathbf{H}'_{\text{ret}}\mathbf{H}_{\text{conv}}\mathbf{H}_{\text{interp}}$ accounts for the proper vertical–horizontal interpolation, obtained through the interpolation operator $\mathbf{H}_{\text{interp}}$, and for the proper unit conversion, obtained through the conversion operator $\mathbf{H}_{\text{conv}}$.

The strengths of the assimilation approach proposed by Migliorini are to be found in the lower computational load with respect to traditional radiance assimilation and in the fact that all the sensor characteristics (spectral resolution, instrument noise, apodization, etc.) are embedded in $\mathbf{y}'_{\text{ret}}$ and $\mathbf{H}'_{\text{ret}}$; therefore, they are transparent to the assimilation system. Therefore, a single module can be used to assimilate equivalently data from different high-spectral-resolution sensors from current (NPP and

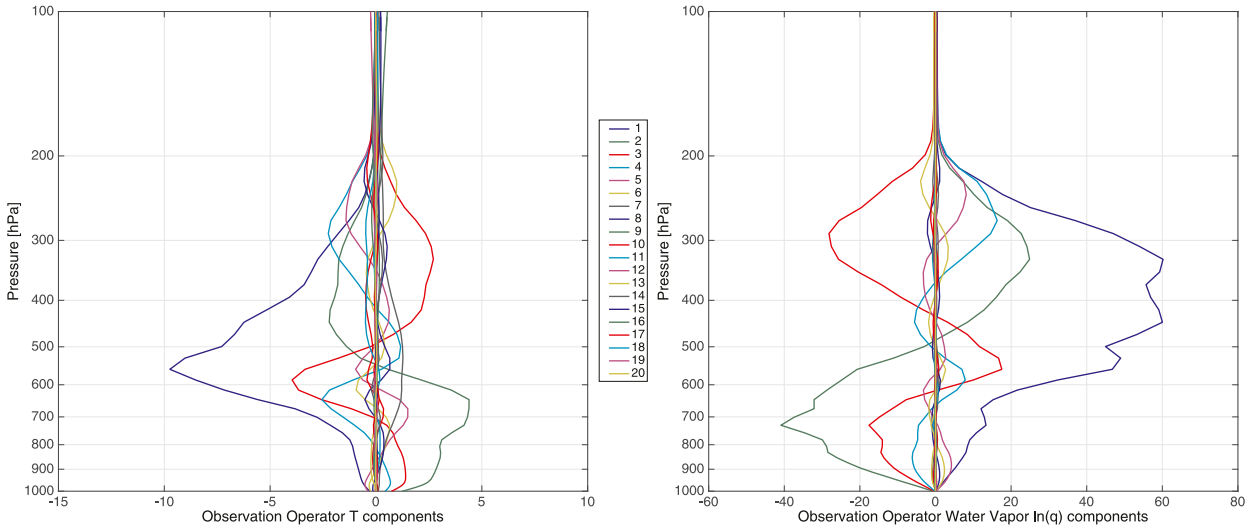

FIG. 6. (left) Temperature and (right) water vapor components of the observation operator $\mathbf{H}'_{\text{ret}}$. Each colored curve represents the two components of the ith row (numbered in the legend) of the observation operator.

MetOp) and future [Joint Polar Satellite System (JPSS) and MTG] platforms.

Preliminary results obtained assimilating SPS into regional models are described in Antonelli et al. (2015), De Haan et al. (2015), and Prates et al. (2016).

3. Implementation of the regional service

The automated system for nearly real-time retrievals of CrIS data, implemented around Mirto, allows for Internet publishing of the results with timeliness of less than 60 min with respect to the overpass time. The inversion of CrIS data relies on the direct broadcast capabilities available at the University of Hawai'i at Mānoa and on the operational modeling activities of the MKWC. The system produces level 2 and level 3 products over the region that span from 19.5°N to 23.5°N and from 150°W to 165°W. Retrievals are generated for the a.m. and p.m. overpasses of the *Suomi NPP* spacecraft, which occur around 0000 and 1200 UTC. (Subsets of level 2 data for the latest overpass are available at http://mkwc.ifa.hawaii.edu/satellite/polar-skewt.cgi, while previous overpasses are available at http://mkwc.ifa.hawaii.edu/archive/satellite/polar-skewt.cgi.) The system generates and posts on the MKWC website maps showing, for each 1° × 1° box, one red or yellow dot indicating the location of one clear-sky retrieval if available within that box. Dots are superimposed to the VIIRS true color image for daytime overpasses (Fig. 7) and to the VIIRS day–night band (DNB) image for the night ones (Fig. 8). Each dot is linked to a skew-T plot of the retrieved profiles and of the 12-h WRF forecast closest to the satellite overpass used as the inversion a priori (Fig. 8c). The skew-T diagram also includes the rawinsonde profiles if the retrievals' FOV falls within 75 km from the radiosounding launch locations. Yellow dots show the location of the retrievals for the closest FOV to the radiosounding location's launch. This product is meant to be used routinely by the MKWC forecaster; therefore, only a representative subset of the retrieved profiles is displayed. Maps of level 3 data such as CAPE, LI, and precipitable water (PW) are also available (http://mkwc.ifa.hawaii.edu/satellite/polar/cris.cgi). The instability indices for all the available retrievals are mapped on the VIIRS image (Fig. 9).

For any individual CrIS FOV, Mirto is currently set up to use a subset of 864 unapodized CrIS radiances (out of the 1305 nominal channels) selected by applying Rodgers' method based on individual channel information content as defined in Eq. (2.77) of Rodgers (2000).

In situ observations providing information on atmospheric stability over the central Pacific area are sparse, with the main ones being the twice daily rawinsondes profiles. Atmospheric instability is of great importance to any forecasting facility and is more so for the MKWC. The center, in fact, besides alerting the telescope facilities on Mauna Kea of approaching bad and hazardous weather conditions, is in charge of accurately predicting fair weather conditions. Telescope operators can maximize telescope usage by employing instrumentation matched to the expected weather conditions. Atmospheric stability plays an important role for the MKWC forecaster and, therefore, for the astronomy community as it is closely related to atmospheric optical turbulence,

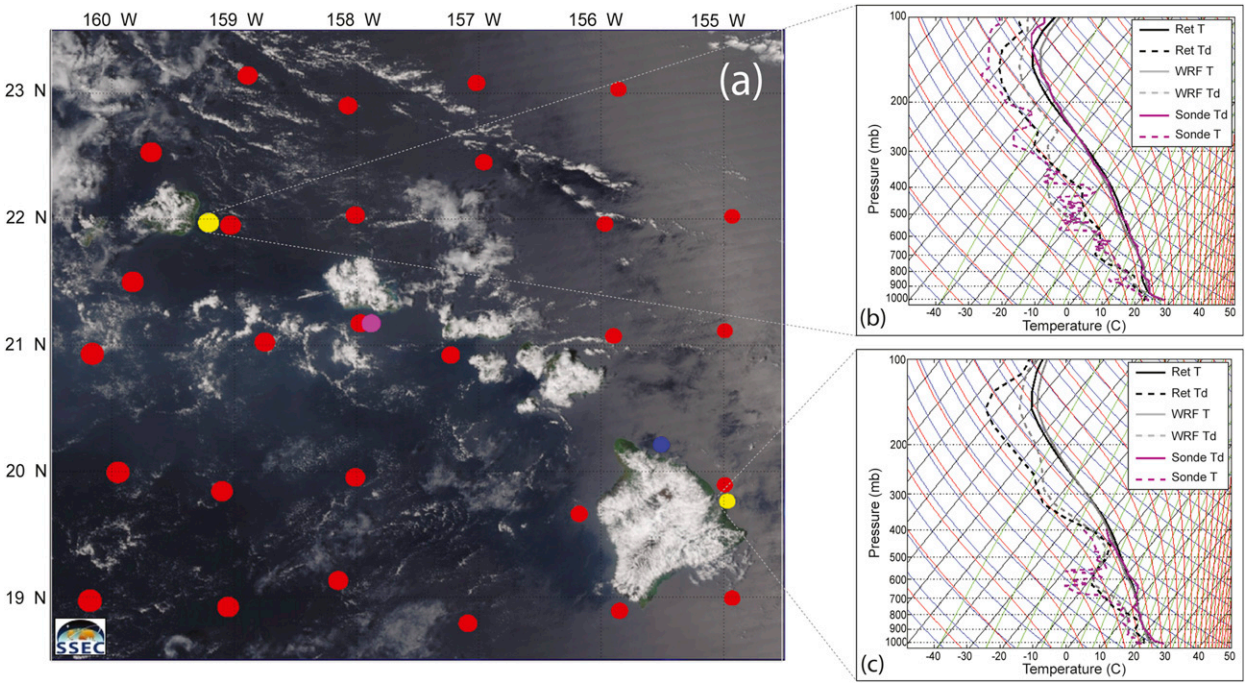

FIG. 7. (a) CrIS retrieval locations superimposed on VIIRS true color image for 2319 UTC 7 Sep 2015. Each dot is linked to a skew-*T* plot of the retrieved (black solid line) and the 12-h WRF forecast validating at the satellite overpass time used as retrieval a priori (gray dashed line) profiles. Sonde profiles (magenta dashed line) are added to the skew diagrams linked to the yellow dots marking the closest retrieved profiles' locations to (b) Lihue and (c) Hilo soundings.

the phenomenon responsible for telescope image degradation. The implemented system provides a particularly valuable tool to analyze and diagnose atmospheric stability over Hawaii using CrIS and more so when IASI retrievals are added.

A close look at Figs. 7 and 8 reveals an interesting discrepancy aloft. Analyses of the retrievals indicate a systematic bias of the WRF Model 12-h forecast with respect to rawinsonde in both temperature and particularly in upper-tropospheric dewpoint (relative humidity). This bias is confirmed by the validation analysis presented in the next section and has been consistently present since the beginning of the operative implementation (section 4).

For the night overpass, Fig. 8 shows three blue dots corresponding to the three FOVs closest to the grid summit location under clear conditions and for convergent retrievals. The corresponding skew-*T* diagrams provide diagnostic, as opposed to forecast, information on the temperature and relative humidity conditions for the lowest atmospheric layers above the summit. These observations differ as expected from the rawinsonde information from Hilo, Hawaii, at those same levels and provide useful guidance for the forecast of summit conditions.

The meteorological scenario on 7 and 8 September 2015 was characterized by persistent midlevel moisture to the west of the Hawaiian archipelago, coupled with a fresh influx of tropical moisture drawn toward the state of Hawaii by an upper-level low developing to the west and Hurricane Jimena weakening to the northeast. Rawinsondes–retrievals in Hilo and Lihue, Hawaii, reveal a weak or indistinct trade wind inversion and a large amount of moisture available in the atmosphere (Fig. 7). The retrievals allow the instability to be assessed throughout the domain. The derived stability patterns show an atmospheric river of moist unstable air impacting the main Hawaiian Islands on 7 and 8 September 2015 (Zhu and Newell 1994).

4. Validation

The goal of the validation analysis is to demonstrate that the satellite retrieval system is able to improve the characterization of the atmospheric state provided by the 12-h WRF forecast used as a priori in the retrieval process. Mirto retrievals, used for validation, over the central Pacific area were generated for 480 overpasses within a period of time that ranges from May 2014 to September 2015. The validation compares the Mirto retrievals and the a priori (WRF Model) with available in situ measurements. Currently, level 2 and level 3 products generated from CrIS data are being routinely validated against GPS data (PW) and rawinsondes (temperature

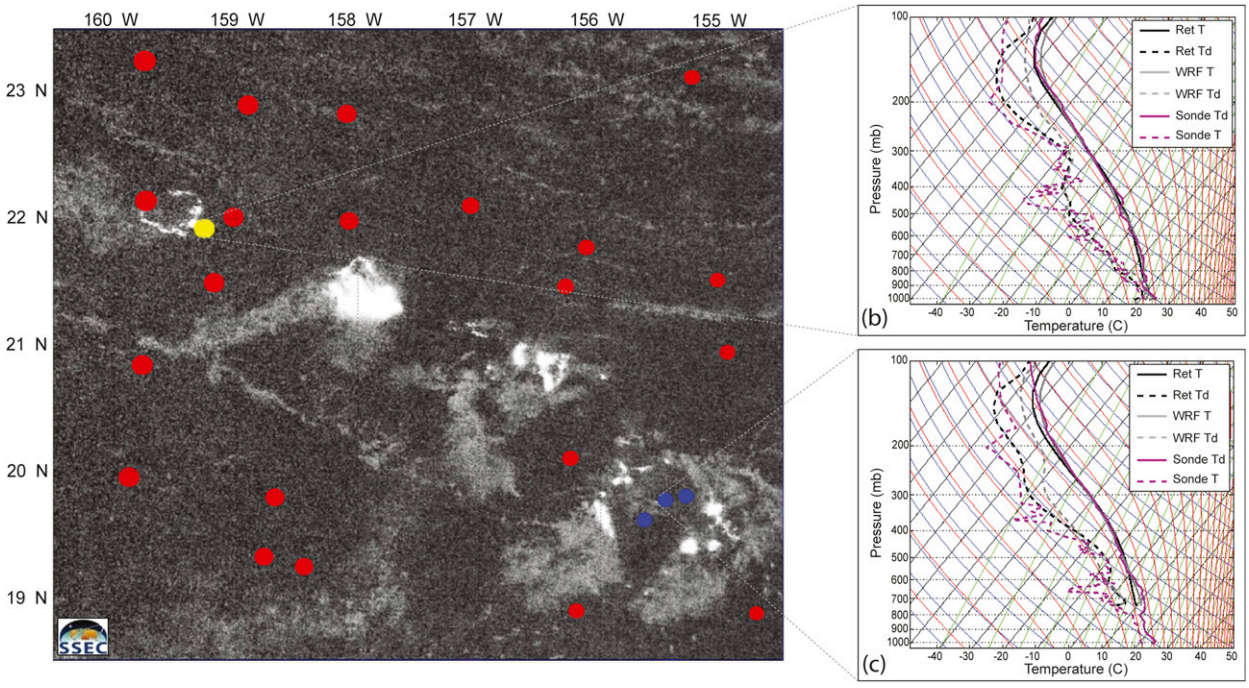

FIG. 8. As in Fig. 7, but for 1148 UTC 7 Sep 2015.

and water vapor) launched at Hilo and Lihue. In addition, retrieval residuals are monitored for each overpass to ensure that the Bayesian inversion is properly done.

a. GPS TPW

A handful of GPS ground stations provide real-time TPW data, which can be used in the validation procedure. The stations used in this study are Honolulu, Hawaii (latitude: 21.31°; longitude: −157.92°), Kauai, Hawaii (latitude: 21.98°; longitude: −159.76°), Hawi, Hawaii (latitude: 20.25°; longitude: −155.88°), and Mauna Loa, Hawaii (latitude: 19.54°; longitude: −155.58°; elevation: 3429 m), as shown in Fig. 10. Another station is available in Hilo, but because of the high average cloud coverage, it has not been used to validate retrieved profiles. For each overpass, TPW from the retrieved profiles of the field of view within 75 km and with surface pressure within 100 hPa (50 hPa for Mauna Loa) from the GPS station site location/pressure has been calculated and compared with the TPW estimated by the GPS stations. The comparison consistently shows that Mirto increases the linear correlation and reduces the root-mean-square differences between GPS TPW and the background TPW (derived from the WRF a priori) (Figs. 11 and 12). Particularly interesting are the results obtained for the high-elevation station located on Mauna Loa, where the retrieval improves significantly the WRF a priori estimate of the upper atmospheric water vapor content, as shown by the smaller spread of the data distribution in the corresponding scatterplot.

b. Rawinsondes

Validation of retrieved temperature and water vapor with rawinsonde observations is often controversial without dedicated sondes launched before and after satellite overpass and without auxiliary instrument to properly characterize the *true* atmospheric state (Tobin et al. 2006). The comparison of the punctual high-vertical-resolution sonde observations with the broad-spatial- and lower-vertical-resolution retrievals may, and often does, lead to ambiguous results. Besides the different spatial and vertical resolutions, the comparison between Mirto retrievals and rawinsondes is polluted by time differences between satellite overpass and actual sonde observation time; potential contamination of retrievals by clouds (cloud mask algorithm based on VIIRS cloud mask is under development); distance between observations associated to *successful* retrievals and rawinsonde; and finally, by rapidly changing topography near the launching stations of Hilo and Lihue. To mitigate these issues, two ad hoc procedures were adopted.

1) COMPARISON WITH RAWINSONDES IN PRESSURE DOMAIN

For 480 CrIS overpasses, M available rawinsondes were compared with all of the retrievals (and relative a priori) that 1) were within 50 km from rawinsonde sites, 2) reached convergence, 3) had maximum relative humidity less than 98%, and 4) had surface pressure greater

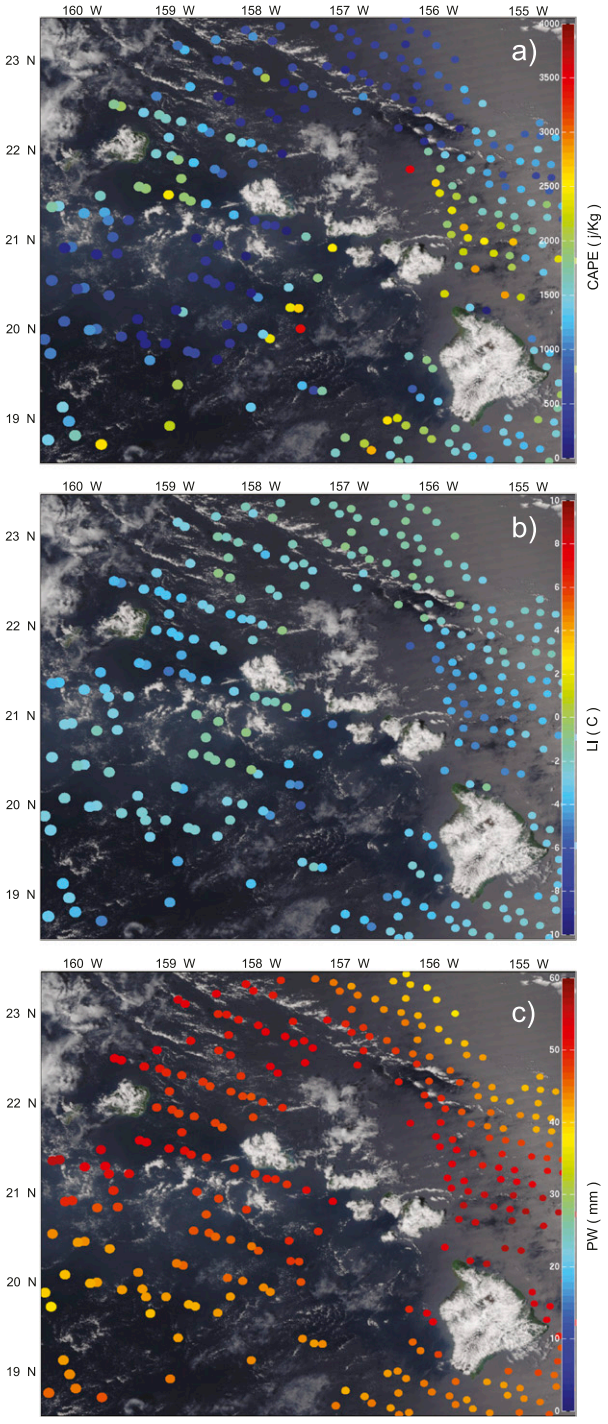

FIG. 9. L3 products derived from CrIS retrievals superimposed on VIIRS true color image on 2319 UTC 7 Sep 2015. (a) Total PW, (b) LI, and (c) CAPE.

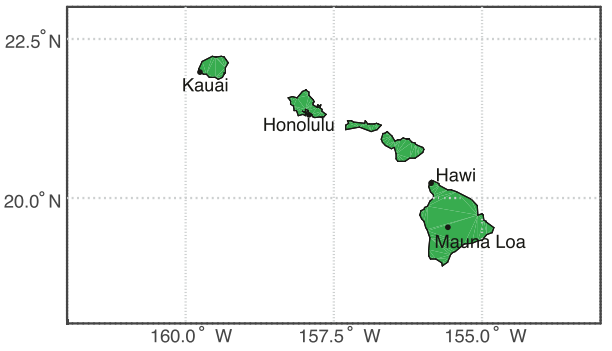

FIG. 10. GPS station locations.

than 900 hPa. To make the comparison, the rawinsonde profiles were also screened for potential saturation (relative humidity $< 98\%$) and were interpolated on the retrieval (a priori) vertical pressure grid. For each pressure level, $i = 1, \ldots, L$, where L is the total number of vertical levels, the root-mean-square differences

$$\mathrm{RMS}_i^{\mathrm{posterior}} = \sqrt{\sum_{j=1}^{M} \frac{(s_{i,j} - \langle \hat{x}_{i,j} \rangle)^2}{M}} \quad \text{and} \tag{16}$$

$$\mathrm{RMS}_i^{\mathrm{prior}} = \sqrt{\sum_{j=1}^{M} \frac{(s_{i,j} - \langle x_{o,i,j} \rangle)^2}{M}}, \tag{17}$$

between the rawinsonde field s_j and the mean of the available retrieval corresponding field ($\langle \hat{x}_j \rangle$) and between the rawinsonde s_j and the mean of the corresponding a priori ($\langle x_{o,i,j} \rangle$) fields were calculated for all available cases for Lihue and Hilo (Figs. 13 and 14). The left and center panels of Figs. 13 and 14 show the results for two independent atmospheric variables: temperature and water vapor mixing ratio, respectively. However, since the radiative transfer (forward model) is sensitive to a combination of these two states and since the water vapor mixing ratio rapidly decreases in magnitude with the altitude, it was chosen to show the comparison results also in terms of relative humidity (right plots), which, by its own formulation, combines T and q and is always within the range 0%–100% throughout the whole atmosphere.

With no cloud mask available to be applied to the observations before and/or after the inversion process, the potential cloud contamination was screened for by eliminating nonconvergent retrievals and convergent profiles with relative humidity $> 98\%$.

Results over Lihue, calculated over 938 CrIS retrievals averaged around $M = 189$ rawinsondes, show that the retrieval process reduces the a priori water vapor mixing ratio root-mean-square (RMS) above the altitude corresponding to 900 hPa. Largest improvement occurs between 850 and 750 hPa, just at the trade wind inversion base height estimated by Cao et al. (2007) around 2000 m (800 hPa). Below 950 hPa, however, it is possible to spot a small degradation of the a priori water vapor mixing ratio RMS. Also, in temperature, a degradation of the posterior

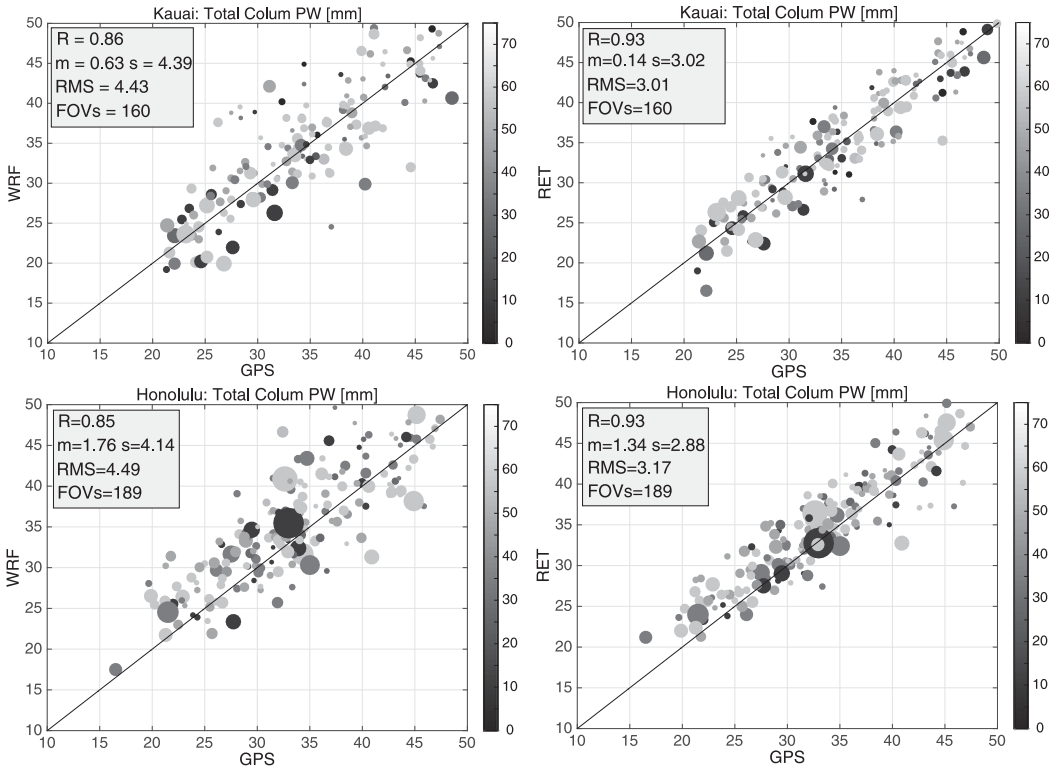

FIG. 11. (left) Scatterplots between GPS- and WRF-derived TPW and (right) the GPS- and retrieval-derived TPW for (top) Kauai and (bottom) Honolulu. Marker size is inversely proportional to FOV distance from the GPS station locations. Shading darkness is inversely proportional to time distance between the GPS and the satellite overpass times. The quantity R represents the linear correlation between GPS and WRF–retrieval values of TPW. The values m, s, and RMS represent the mean, standard deviation, and RMS of the differences GPS and WRF–retrieved TPW, respectively. The value FOVs represents the number of observations plotted and used to derive the statistics.

RMS is visible between 180 and 300 hPa. However, the small degradations disappear in the relative humidity plots on the right, suggesting again that the retrieval optimizes the combined effect of water vapor mixing ratio and temperature rather than the individual components. Overall relative humidity a posteriori RMS differences are about 10% everywhere except for a peak around the top of the boundary layer (around 800 hPa), where higher variability is expected, and with a consistent improvement with respect to the a priori RMS particularly pronounced around 200 hPa.

Results over Hilo (Fig. 14), obtained by averaging 301 retrievals over $M = 108$ rawinsondes, seem to confirm the conclusions drawn from Fig. 13. The posterior temperature RMS is worse than the prior one between surface and the altitude corresponding to 850 hPa, and also, the posterior water vapor mixing ratio RMS is worse than the prior one between 900 and 800 hPa. However, the posterior RMS in terms of relative humidity is shown to be smaller or equal to the prior RMS for the same vertical regions. Similar effects are also shown between 600 and 400 hPa and 250 and 180 hPa, where, despite having larger RMS in temperature, the retrieval improves the relative humidity RMS. As for Lihue, above the top of the boundary layer (around 800 hPa), the posterior relative humidity RMS differences are about 10%.

It is also worth mentioning that over Hilo, the median cloud cover ranges from 63% to 83% (https://weatherspark.com/averages/33129/Hilo-Hawaii-United-States), while over Lihue, it ranges from 57% to 73% (https://weatherspark.com/averages/33119/Lihue-Hawaii-United-States).

Given these numbers, it is possible to speculate that, for observations with higher probability of being only partially contaminated by clouds (small cloud fraction within FOV), the retrieval process can still provide the proper combination of temperature and water vapor, but does not perform as well in getting the correct individual values as they are diversely conditioned in the a priori matrix, which has been defined for clear-sky-only pixels.

2) COMPARISON WITH RAWINSONDES IN PRINCIPAL COMPONENT DOMAIN

Rawinsondes have much higher vertical resolution with respect to NWP model and retrieved profiles;

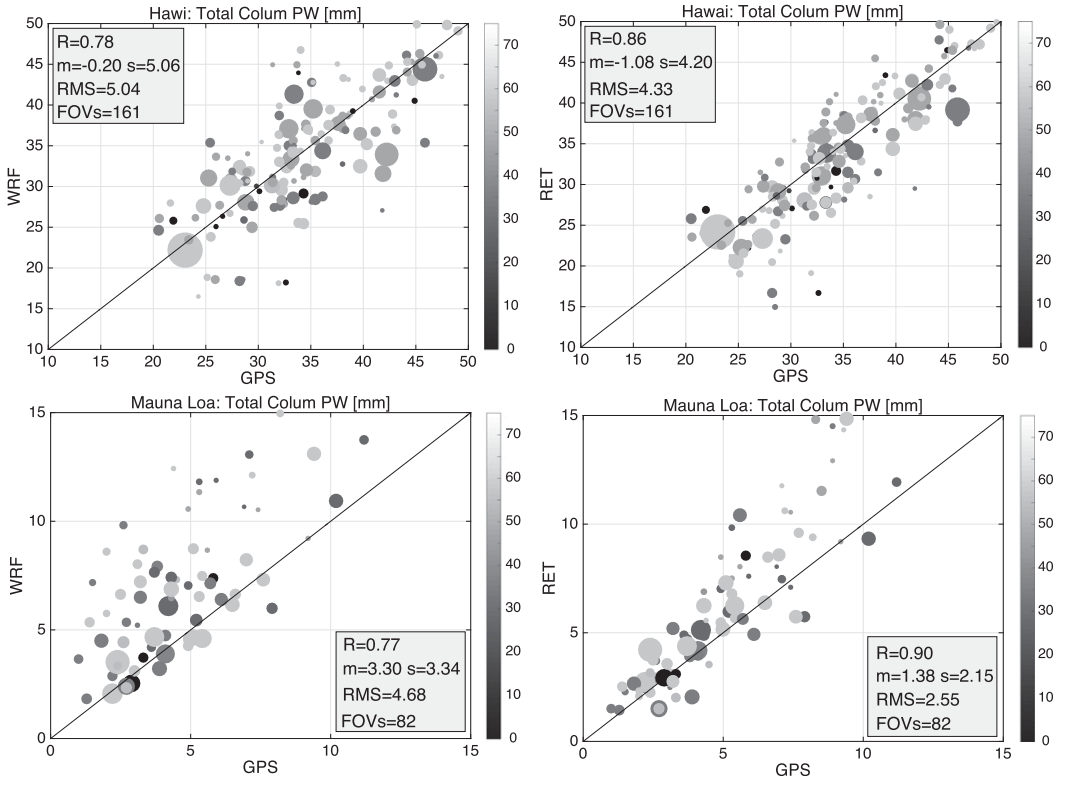

FIG. 12. As in Fig. 11, but for (top) Hawi and (bottom) Manua Loa.

therefore, the comparison level by level only provides limited information on the effective differences between the profiles. For this reason, a comparison in the rawinsonde principal component space is investigated. The basic idea is to derive the principal components (PCs) from a relatively large set of rawinsondes and to use different numbers of them, as basis functions, to represent both sondes and retrievals (along with the a priori) with different degrees of explained variance.

The covariance of the rawinsonde profiles is defined for each variable as

$$\mathbf{C} = E[(\mathbf{S} - E[\mathbf{S}])(\mathbf{S} - E[\mathbf{S}])^{\mathrm{T}}], \tag{18}$$

where $\mathbf{S}$ is an atmospheric field such as temperature, water vapor mixing ratio, or relative humidity observed or derived from the rawinsonde. The idea is to use the empirical orthogonal functions, or PCs, generated by diagonalizing the covariance $\mathbf{C}$ of the rawinsonde profiles,

$$\mathbf{C} = \mathbf{U}\boldsymbol{\Xi}\mathbf{V}^{\mathrm{T}},$$

to calculate the RMS differences in Eqs. (16) and (17) as function of N_t, the number of PCs (columns of the left eigenvectors $\mathbf{U}$, or rows of the right eigenvectors $\mathbf{V}^{\mathrm{T}}$, associated to the N_t, largest eigenvalues $\boldsymbol{\Xi}$ of $\mathbf{C}$), used to represent the profiles

$$\mathrm{rms}_i^{\mathrm{posterior}}(N_t) = \sqrt{\sum_{j=1}^{M} \frac{\left[\sum_{q=1}^{N_t} (\phi_{j,q} - \hat{\psi}_{j,q}) U_{i,q}\right]^2}{M}} \quad \text{and} \tag{19}$$

$$\mathrm{rms}_i^{\mathrm{prior}}(N_t) = \sqrt{\sum_{j=1}^{M} \frac{\left[\sum_{q=1}^{N_t} (\phi_{j,q} - \psi_{oj,q}) U_{i,q}\right]^2}{M}}, \tag{20}$$

where

$$\phi_{j,q} = \sum_{i=1}^{L} s_{j,i} U_{i,q},$$

$$\hat{\psi}_{j,q} = \sum_{i=1}^{L} \hat{x}_{j,i} U_{i,q}, \quad \text{and}$$

$$\psi_{0j,q} = \sum_{i=1}^{L} x_{0j,i} U_{i,q}, \tag{21}$$

and $j = 1, \ldots, M$; $i = 1, \ldots, L$; $q = 1, \ldots, N_t$ are respectively the amplitudes of the jth rawinsondes, of the jth mean retrieval, and of the WRF jth mean a priori,

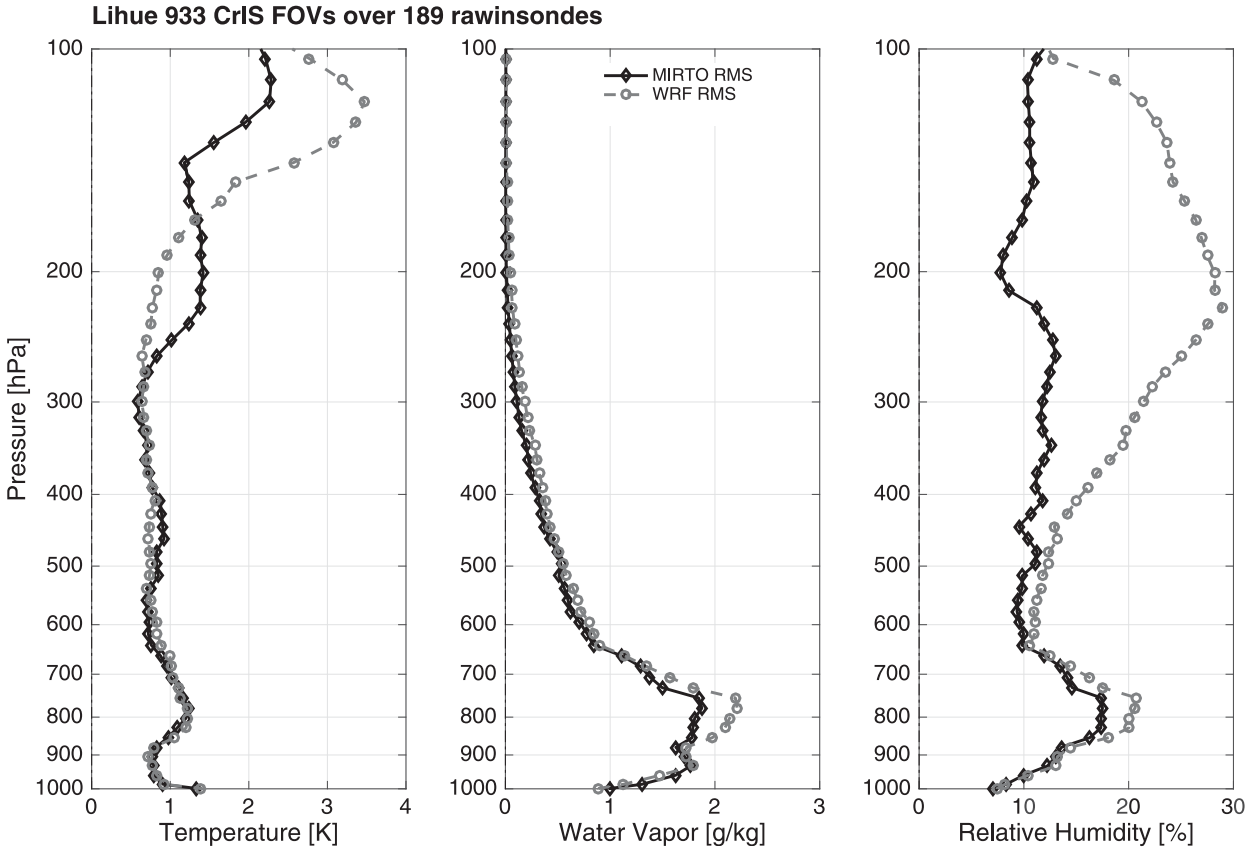

FIG. 13. Comparison of Mirto (black solid line) and WRF (dashed gray line) profiles with collocated rawinsondes launched from Lihue. Shown are the RMS errors for (left) temperature (K), (center) water vapor mixing ratio (g kg^{-1}), and (right) relative humidity (%).

projected onto the qth individual PC (column of $\mathbf{U}$). The lower-order PCs (corresponding to the largest eigenvalues in $\mathbf{\Xi}$) are those that explain most of the profile variance and have lower vertical resolution with respect to the higher-order ones.

Since only a limited number of independent pieces of information are embedded in the observations, about 5–6 for water vapor and 10–12 for temperature calculated according to Eq. (2.50) of Rodgers (2000), it is qualitatively expected that above those numbers, the distance between the rawinsondes and the retrieved/forecast profiles increases. The word "qualitatively" here indicates that, being the PCs derived from the rawinsonde and those derived independently for each variable, they do provide only a suboptimal base to represent the information content of the retrievals.

Three years of rawinsonde data for each station were collected. The sonde profiles were then interpolated on a common pressure grid with $L = 100$ levels ranging from 1015 hPa to 0.1 hPa and used to generate the PCs for temperature, water vapor mixing ratio, and relative humidity (Fig. 15).

The same data used in the previous section were selected, projected, and reconstructed using different numbers N_t of PCs. RMS values of the differences between the reconstructed retrievals and reconstructed rawinsonde ($\text{rms}^{\text{posterior}}$) and between reconstructed a priori and reconstructed rawinsondes ($\text{rms}^{\text{prior}}$) were then calculated for different number of PCs used in the reconstructions. Figure 16 shows that, when using only one PC, for both Hilo and Lihue, the reconstructed retrievals (dark solid line with diamonds) are in better agreement with the reconstructed rawinsondes than the first guess (gray dashed line with circles). The thin dashed line indicates the *reconstruction error*, that is, the RMS differences between the full vertical resolution rawinsonde and the one reconstructed using only one PC. This seems to indicate that Mirto properly *moves* the basic vertical structure of the WRF Model (a priori) toward the rawinsonde. Figure 17, obtained using the first five PCs, shows a similar behavior, but now in the boundary layer, $\text{rms}^{\text{posterior}}(N_t = 5)$ and $\text{rms}^{\text{prior}}(N_t = 5)$, after the reconstruction, are almost equivalent. This indicates that, as N_t increases and the reconstruction error decreases, the RMS of the differences is more and more dominated by the differences of vertical resolution between the rawinsonde and the retrieved/forecast profiles in the portion of the atmosphere with greater variability.

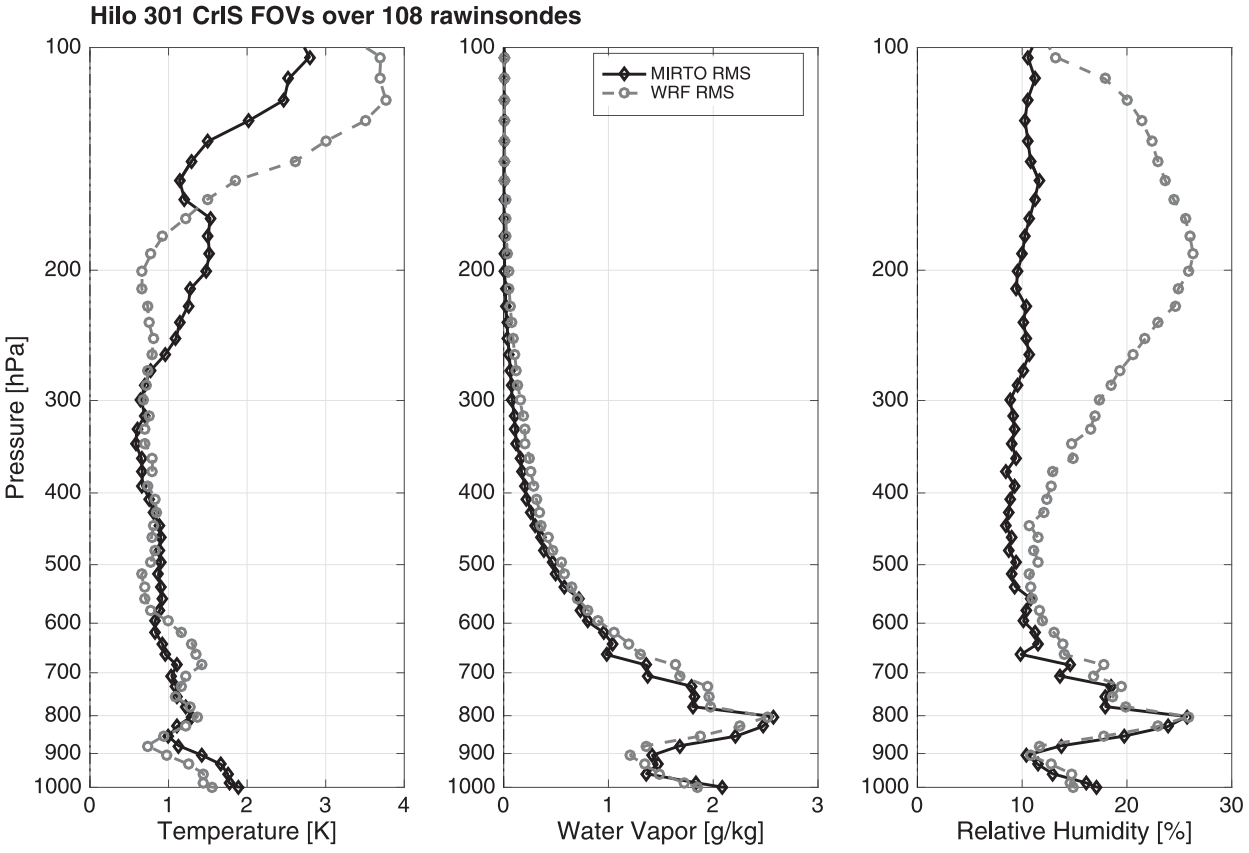

FIG. 14. As in Fig. 13, but for Hilo.

By the time $N_t = 20$, PCs are used (as shown in Fig. 18), and for any number greater than 20 (not shown in the paper), the RMS of the boundary layer water vapor mixing ratio differences assumes the same structures shown in Figs. 14 and 13, which correspond to a reconstruction based on all the available PCs.

It is worth noting that the PCs in relative humidity have sharper and more localized maxima in the vertical structure with respect to the PCs in temperature and water vapor (Fig. 15). This makes them better suited to demonstrate the consistency of the improvement of Mirto on the WRF a priori as the amount of explained variance and the vertical resolution increase with N_t. In fact, while in temperature and water vapor mixing ratio, the relative magnitude of RMS values changes with N_t so that $\mathrm{rms}^{\mathrm{posterior}}(N_t) \lessgtr \mathrm{rms}^{\mathrm{prior}}(N_t)$ in the relative humidity space $\mathrm{rms}^{\mathrm{posterior}}(N_t) \leqq \mathrm{rms}^{\mathrm{prior}}(N_t)$ for every level and for every N_t, with the equal sign holding true for $N_t \geq 5$ and for the levels in the boundary layer.

Validation of ozone and surface parameters would add valuable information on the behavior of the inversion system; however, since no cloud mask is available at time of writing, it is considered beyond the scope of the article, and it is left to future work.

5. Retrieval diagnostic

A spectral residual analysis has also been carried out to determine whether the behavior of Mirto is correct. Spectral residuals have been consistently proven useful in detecting systematic anomalies in instrument and data processing performances (Tobin et al. 2013; Masiello et al. 2012; Esposito et al. 2007; Hultberg 2009). In addition, the analysis of spectral residuals allows for estimates of relevant variables such as instrument noise (Serio et al. 2015) and calibration artifacts (Han et al. 2013; Strow et al. 2013). In particular, the standard deviation of the spectral residuals, calculated for converging retrievals for a well-behaved system, is expected to approach the random component of the instrument noise (Serio et al. 2015).

The statistics calculated for the spectral residuals obtained from 2500 nonsaturated, converging retrievals is shown in Figs. 19 and 20. In general, the shape of the standard deviation of the residuals follows quite closely

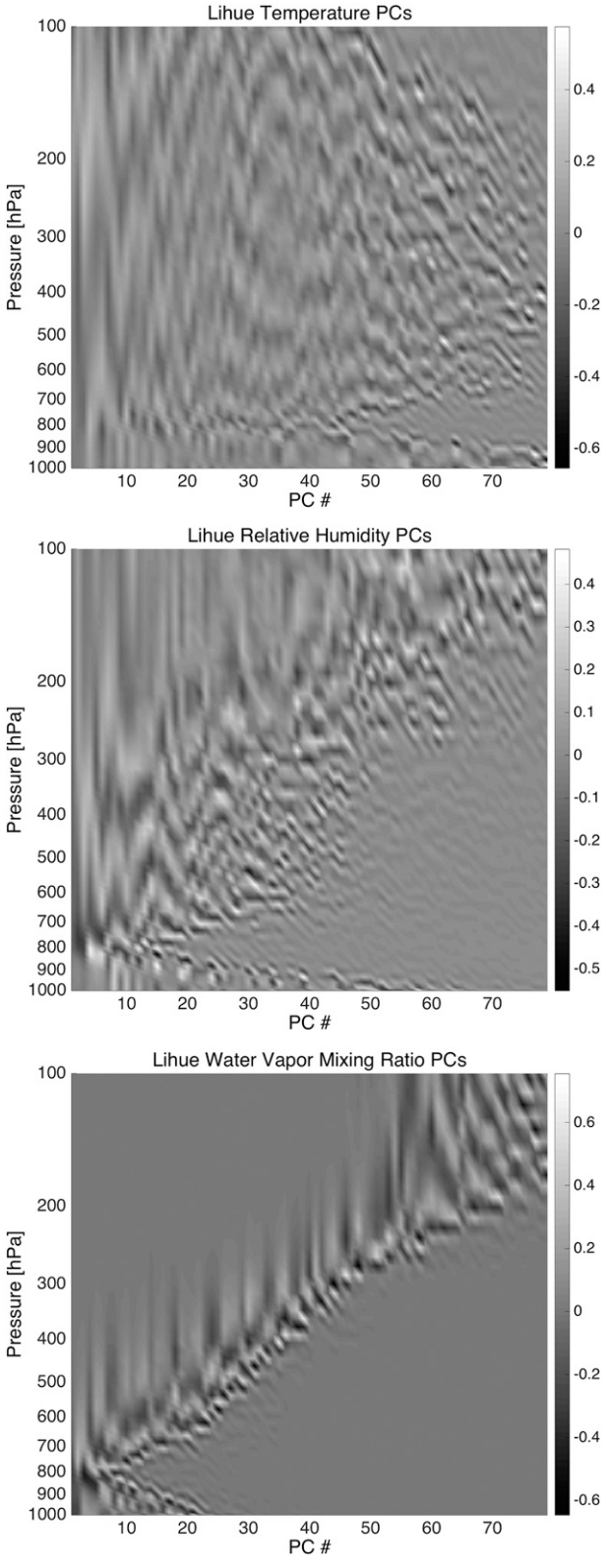

FIG. 15. PCs of (top) temperature, (middle) water vapor mixing ratio, and (bottom) relative humidity derived from all available (clear sky) rawinsondes launched in Lihue between January 2012 and September 2015.

the shape of the instrument noise; however, the inset in Fig. 19 indicates that the random component of the CrIS noise might actually be underestimated with respect to its true value.

In addition to the calculation of the mean and standard deviation, principal component analysis (PCA) of the noise-normalized spectral residuals (Antonelli et al. 2004) has been used as a diagnostic tool. In fact, it helps identify potential sources of error, such as inconsistencies between the observation and the forward model and/or calibration issues. The application of PCA (Figs. 21 and 22) to the 2500 noise-normalized spectral residuals obtained from converging retrievals collected from different overpasses indeed provided two interesting indications of the behavior of the inversion system.

From the analysis of the first 10 PCs for the LW band, a form of *ringing* in the second and third PCs in and around the ozone absorption band is found. The issue with ringing has been investigated and described by Han et al. (2013) and Han (2015).

A second relevant indication comes from the eigenvalues of the covariance of the noise-normalized spectral residuals (Fig. 23). If the residuals were just the random component of the instrument noise, the eigenvalues should have been flat and close to 1. The first eigenvalues being larger than 1 indicate that the spectral residuals still carry spectral information not exploited by the retrieval. This is likely due to the components of the observation error not properly accounted for in the total covariance matrix (forward model error, correlated instrument noise, uncertainties in the distribution of the minor chemical species in the atmosphere, possible cloud contamination, etc.).

Future improvements of the retrieval system, based on improving the observation error and the a priori covariances, will aim to obtain eigenvalues closer to unity. Continuous monitoring of the principal components and of the eigenvalues of the spectral residuals is a powerful diagnostic tool to evaluate the performances of the retrieval system and is planned to be fully implemented in the near future.

6. Conclusions

This paper describes the implementation of a regional service over the Hawaiian Islands that aims to combine weather forecasts with satellite high-resolution infrared observations to provide better characterization of the atmospheric state. The service is based on Mirto, a Bayesian inversion system that provides level 2 products in nearly real time (<60 min from satellite overpass time), including scaled projected states, that is, level 2 products tailored to optimal data assimilation.

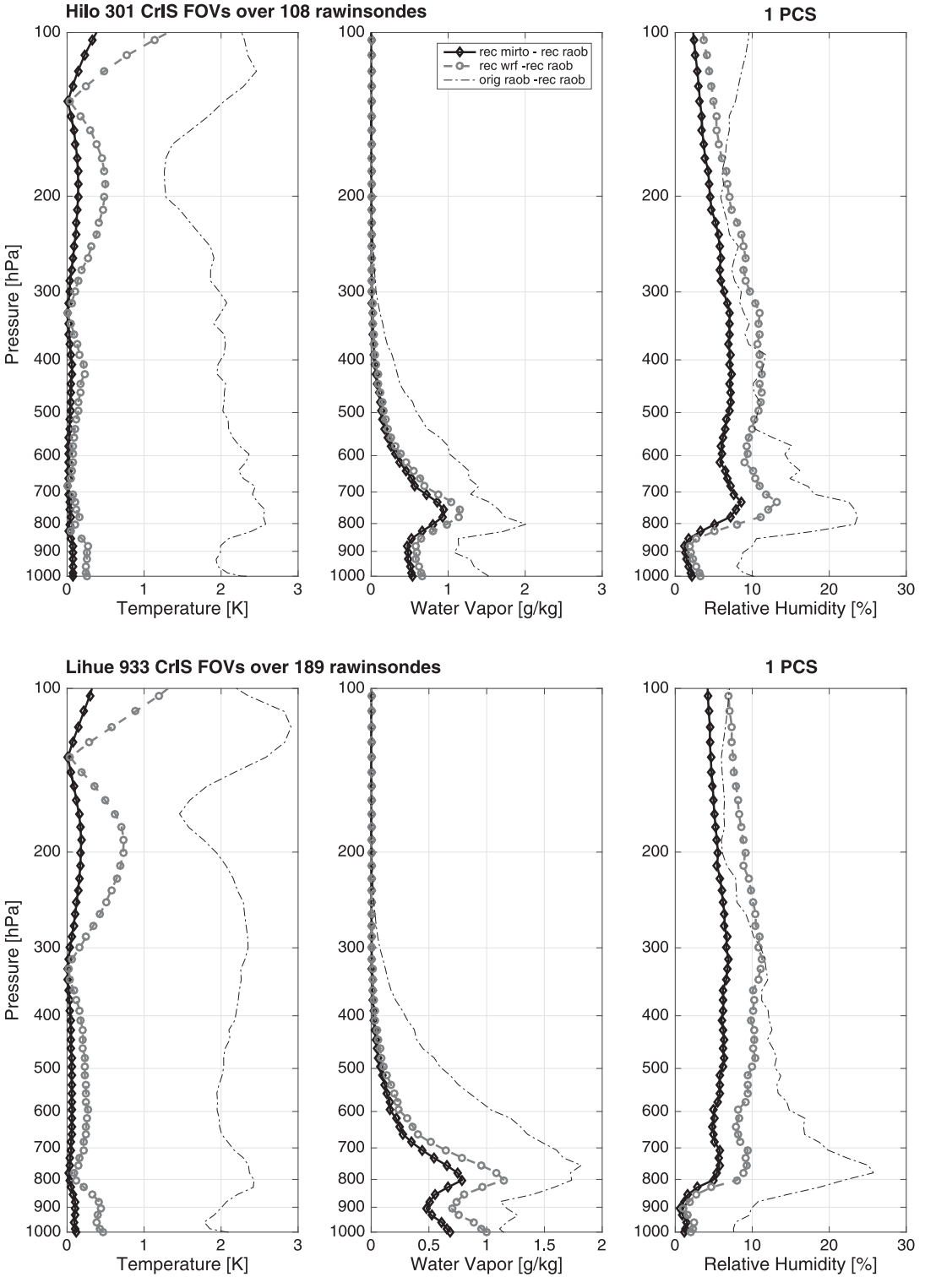

FIG. 16. Comparison of Mirto (solid line) and WRF (dashed line) profiles with collocated rawinsondes launched from (top) Hilo and (bottom) Lihue. Solid dark lines with diamonds represent the RMS difference between retrievals and rawinsonde for temperature (K), water vapor mixing ratio (g kg^{-1}), and relative humidity (%), reconstructed using only one PC. Gray dashed lines with circles represent the same quantities between first guesses and rawinsondes. Solid thin lines represent the RMS of the differences between the original (full vertical resolution) rawinsondes and the reconstructed ones.

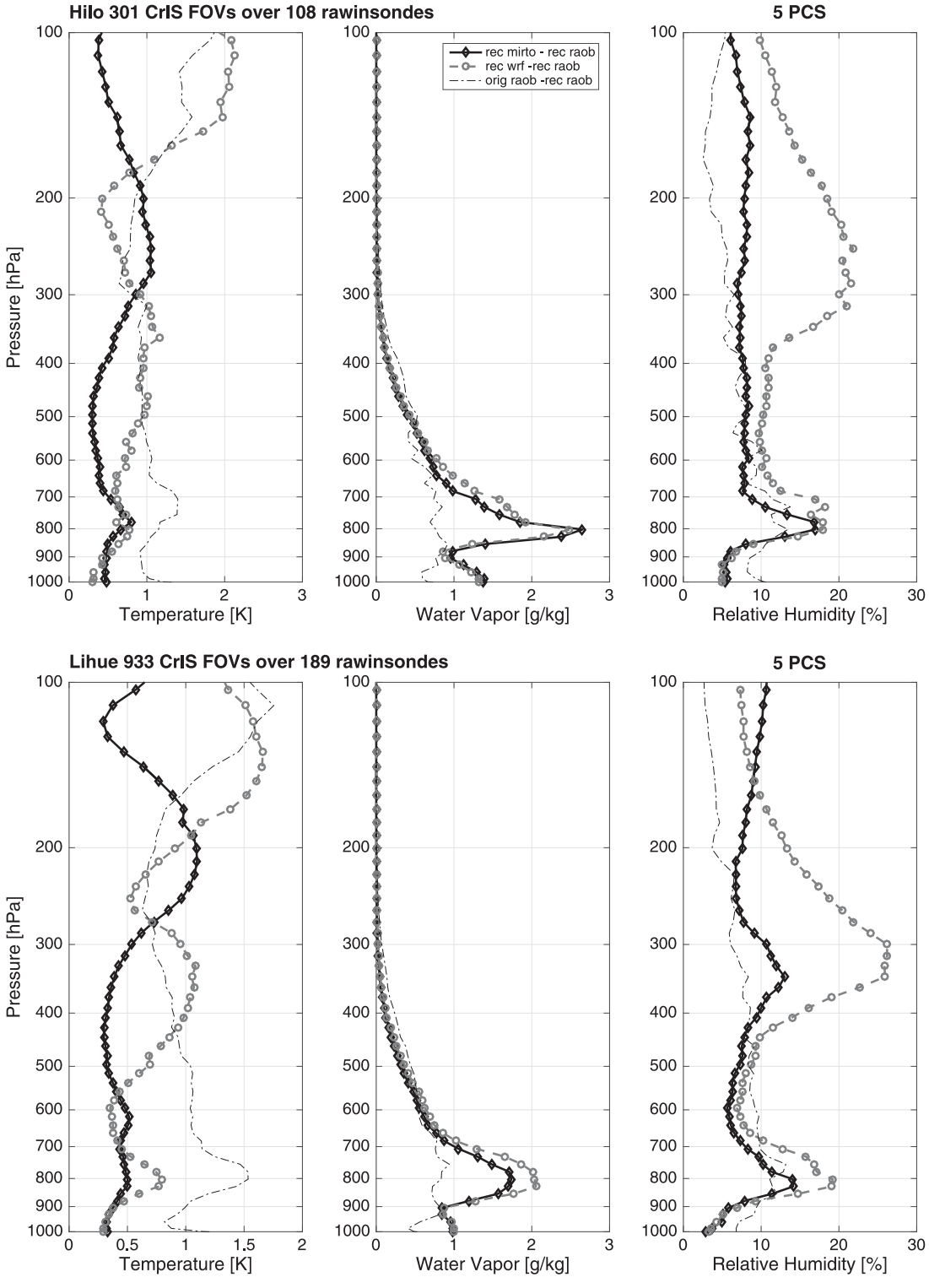

FIG. 17. As in Fig. 16, but reconstructed using the first five PCs.

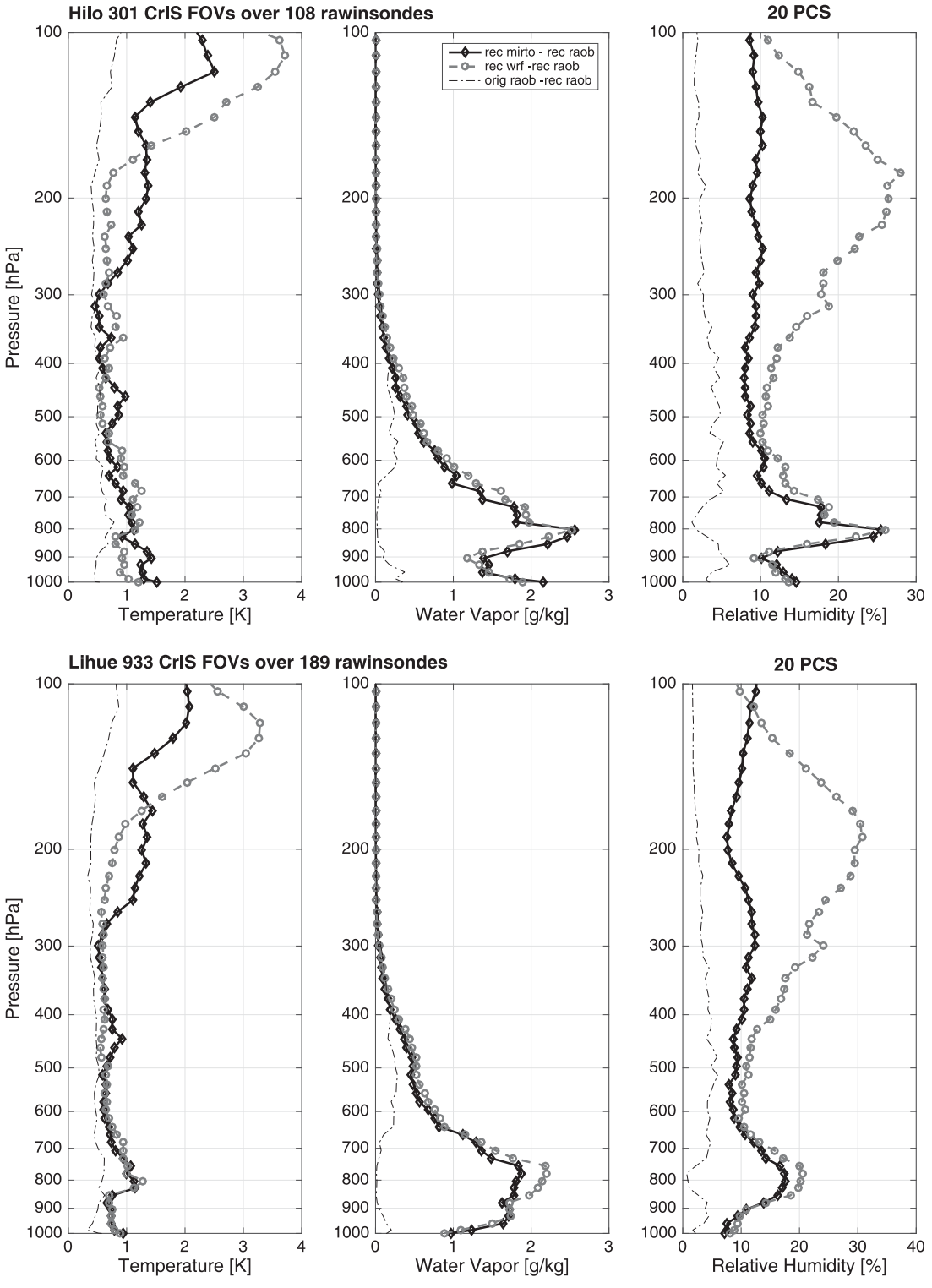

FIG. 18. As in Fig. 16, but reconstructed using the first 20 PCs.

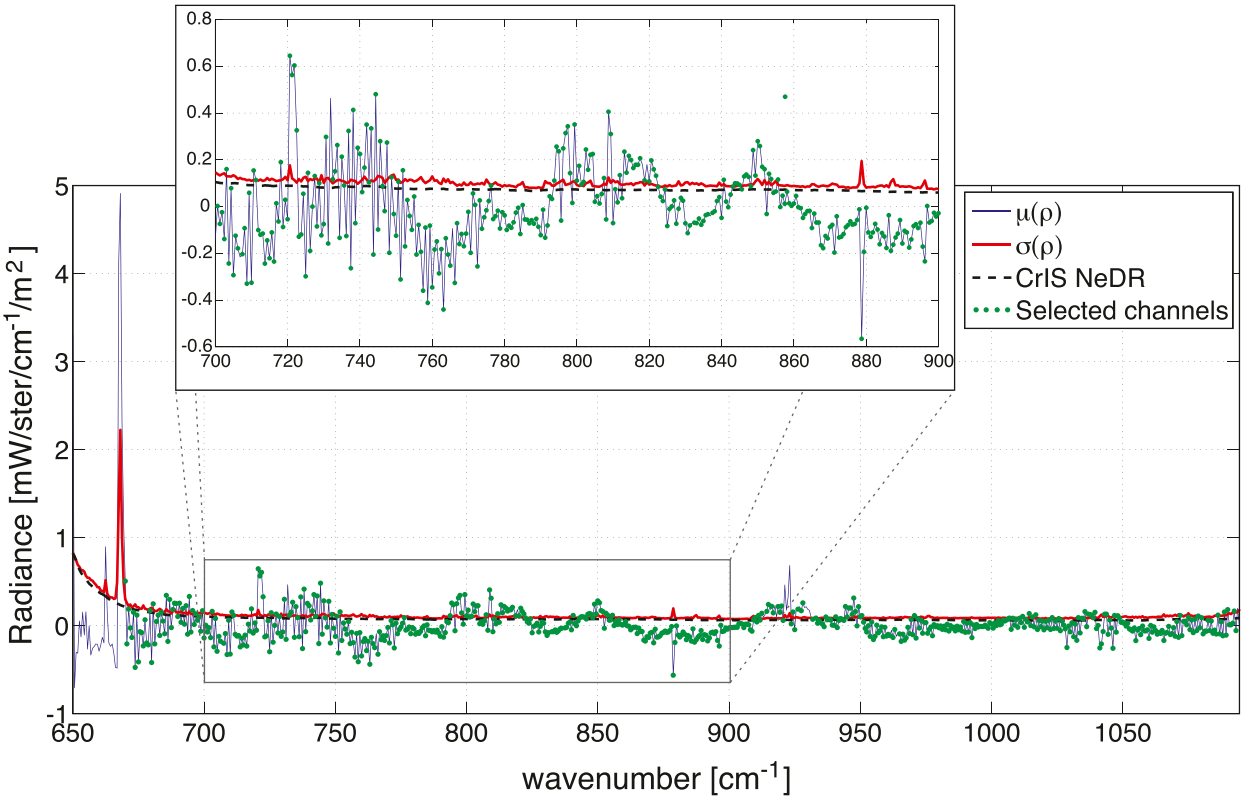

FIG. 19. Comparison of the mean (μ) and the standard deviation (σ) of the spectral residuals (ρ), with the random component of the CrIS noise equivalent radiances (NEDR), for the LW band. The expected value of the residuals μ represents the square root of the diagonal elements of $\mathbf{R_H}$, the systematic error component of the total error covariance matrix used by Mirto. The standard deviation of the residuals σ represents the square root of the diagonal elements of $\mathbf{R}_m$, the instrument noise error component of the total error covariance matrix used by Mirto. Green dots represent the channels used by the retrieval system.

The regional retrieval system runs daily at the Mauna Kea Weather Center in Hawaii. Currently, the system produces CrIS level 2 and 3 output from level 1 data for each overpass of the *Suomi NPP* spacecraft at about 0000 and 1200 UTC daily. Specifically, it provides vertical profiles of temperature and relative humidity and related stability indices on an approximately $6° \times 6°$ grid centered on the Hawaiian archipelago. A coincidence of advantageous factors made this implementation possible and important: (i) the availability of a direct broadcast system operated by the SSEC in collaboration with the National Weather Service and the University of Hawai'i at Mānoa, which provides nearly real-time (about 15 min from satellite overpass time) high-resolution infrared data from the CrIS sensor on *Suomi NPP*; (ii) the availability of operational WRF forecasts at the MKWC, which provide the a priori knowledge of the atmospheric state needed by the retrieval system; and (iii) the paucity of atmospheric observations in the north-central Pacific area.

Following a Bayesian approach, the WRF Model background fields are blended with the physical information present in the satellite observations, resulting in new diagnostic guidance that has been made available on the MKWC Internet pages since August 2013. Besides the retrievals of atmospheric temperature and water vapor, and the generation of some instability indices, the overall relevance of this work relies on the generation of SPS [retrievals transformed according to Migliorini (2012)], which makes the assimilation of retrieved profiles not only possible but computationally efficient.

Previous attempts to assimilate level 2 data did not account for the distorting influence of the a priori background used in the retrieval inversion, making assimilation unsuccessful. With their work, Rodgers (2000) and Migliorini et al. (2008) introduced a transformation method to overcome this issue and properly assimilate retrieved profiles by removing the a priori information from the retrievals.

While national meteorological centers routinely assimilate satellite radiances, Migliorini (2012), by demonstrating the theoretical equivalence between radiance and retrieval assimilation, generated a renewed interest

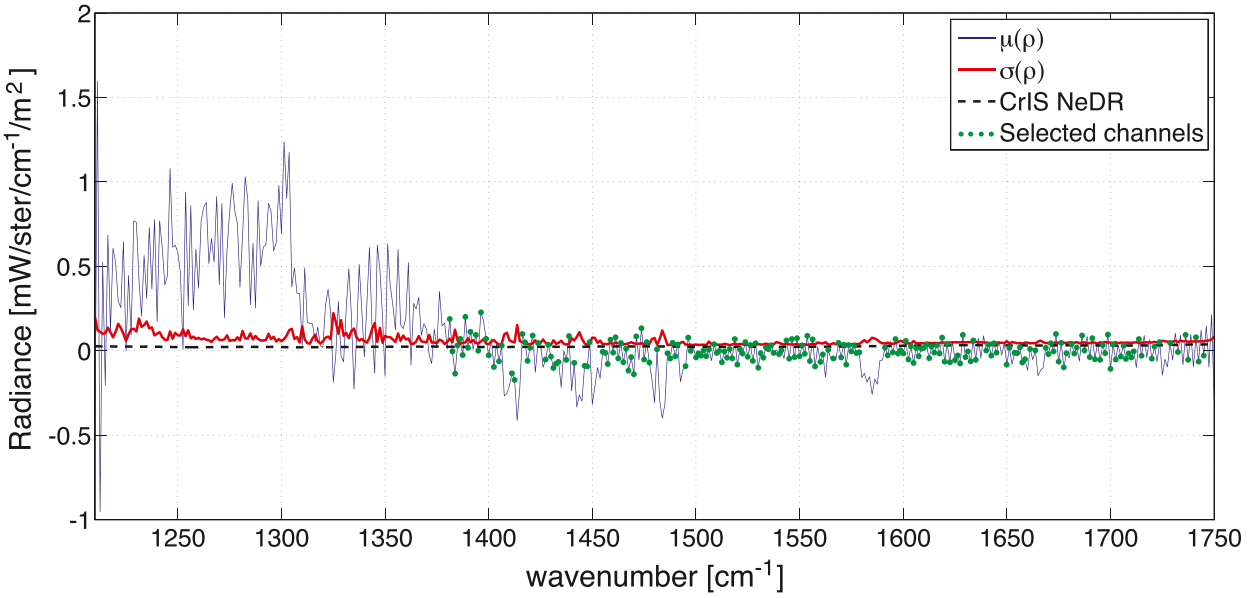

FIG. 20. As in Fig. 19, but for the MW band.

in investigating the use of transformed level 2 data, especially for smaller centers. Radiance assimilation of hyperspectral data, in fact, implies large computational costs and in-depth knowledge of the sensor characteristics, which not every center can afford. In this regard, the use of the transformed retrievals (SPS) bears two important advantages for NWP data assimilation: it requires smaller computational loads, and it makes it possible to treat data from different sensors equivalently. For these reasons, MKWC entered an undergoing project supported by EUMETSAT on the assimilation of SPS, whose results will be presented in a paper currently in preparation.

A validation analysis of the implemented system has been carried out to assess the retrieval accuracy. The results presented in this paper indicate that the information retrieved from the satellite data improves the accuracy of the background state provided by WRF forecasts. Validation results were obtained by comparing both level 2 and level 3 environmental data records (EDRs) CrIS products collocated in time with rawinsondes from Lihue and Hilo (vertical profiles of temperature and water vapor) and with four GPS stations located throughout the Hawaiian Islands (total precipitable water).

The results obtained using rawinsondes were consistent in showing no degradation of retrieved relative humidity with respect to the a priori throughout the entire vertical profile extent. Improvements were found at the top of the boundary layer (trade wind inversion) and in the layers aloft, where the background fields seem to exhibit consistent moisture biases. Improvements in temperature were also shown, but they were less consistent. This is not surprising because temperature is a well-predicted variable by both global and mesoscale models and therefore is not easily improved. Moreover, the inversion system tends to perform better in improving the combination of atmospheric temperature and water vapor (relative humidity) rather than the individual variables.

The results obtained with TPW comparisons showed that Mirto retrievals increase the linear correlation between GPS TPW and the background TPW (WRF a priori) and reduce the root-mean-square differences between GPS TPW and the background TPW (WRF a priori). Particularly interesting are the results obtained

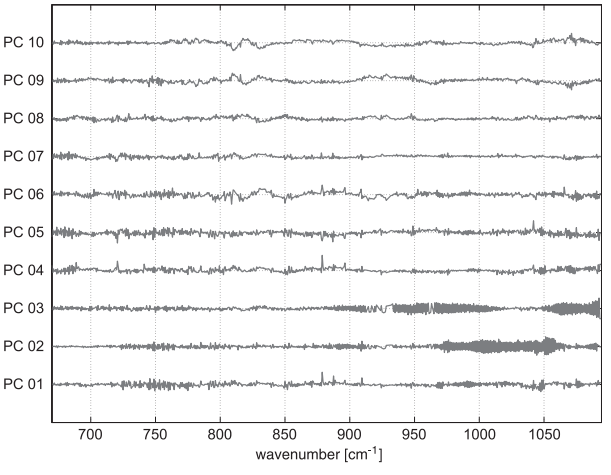

FIG. 21. PCs of the noise-normalized spectral residuals for the LW band.

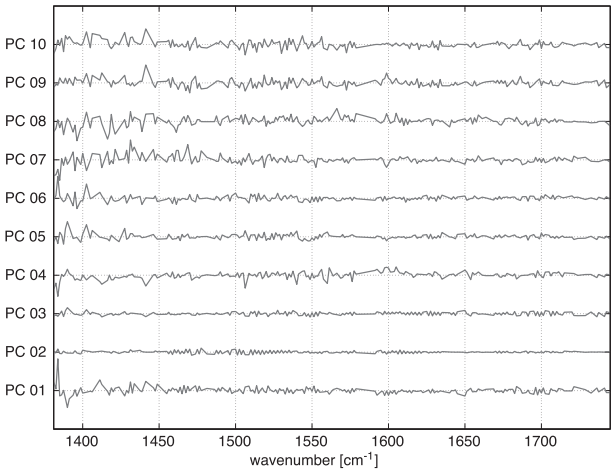

FIG. 22. As in Fig. 21, but for the MW band.

for the high-elevation station located on Mauna Loa, where the retrieval significantly improves the WRF estimate of the columnar water vapor content.

In addition to the atmospheric validation, results from a diagnostic analysis were presented. The analysis was performed by monitoring the spectral residuals for convergent, nonsaturated retrievals. Following Serio et al. (2015), the standard deviation of the spectral residuals was found to properly mimic the instrument noise, while the principal components analysis of the spectral residuals suggested that the whole spectral information embedded in the observations might not yet be fully exploited by the inversion system. This might likely be due to the components of the observation error not explicitly accounted for in the error covariance matrix (forward model error, correlated instrument noise, uncertainties in the distribution of the minor chemical species in the atmosphere, etc.). Future improvements of the retrieval system will aim to obtain eigenvalues closer to unity by improving the characterization of the a priori and the total error covariance matrices. Continuous monitoring of the principal components and of the eigenvalues of the spectral residuals was found to be a powerful diagnostic tool to evaluate the performances of the retrieval system.

Future work

While results from the validation of the Mirto retrieval system are encouraging, more can be done to improve the system by screening the observations for cloud contamination (implementation of a cloud mask) and by improving the characterization of the a priori and of the total error covariances. Therefore, in the near future, the validation will be refined to include comparisons of retrievals and a priori with atmospheric analyses screened for cloud contamination by means of the VIIRS cloud mask collocated with CrIS observations. A denser GPS

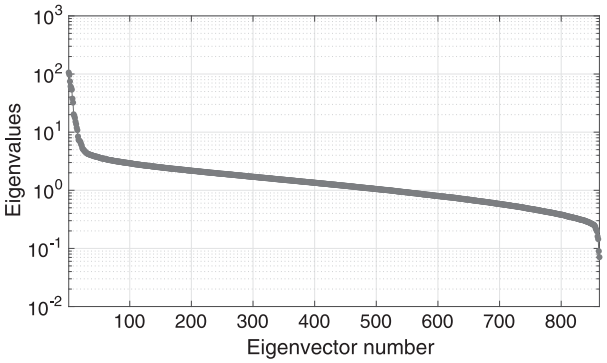

FIG. 23. Eigenvalues of the covariance of the noise-normalized spectral residuals.

dataset available on Mauna Loa will be used to validate the derived TPW over complex terrain. Data from meteorological sensors available on Mauna Kea will also be used to investigate the retrieval performance over the island of Hawaii. Furthermore, the continuous monitoring of the principal components and the eigenvalues of the spectral residuals will allow Mirto algorithm refinement. Once the validation and diagnostic parts of the Mirto system are fully operative, the research will focus on the improvement of the a priori and the total error covariance matrices. Eventually, given the modular nature of the Mirto retrieval system, more sensors will be included as input to the system. In particular, IASI A and B data, given the local overpass times between 2100 and 2200 UTC and 0900 and 1000 UTC, will nicely complement the CrIS overpasses.

Acknowledgments. We thank the Space Science Engineering Center of the University of Wisconsin–Madison and the Mauna Kea Weather Center of the University of Hawaii for supporting the implementation of the regional retrieval system based on Mirto; Atmospheric and Environmental Research (AER) for the use of the optimal spectral sampling forward model; the UCAR Unidata Program for the dissemination of real-time GFS products; the University of Wyoming for their soundings archive; and the MADIS program of NOAA's Office of Oceanic and Atmospheric Research (OAR) Earth System Research Laboratory (ESRL) Global Systems Division (GSD) for the real-time dissemination of the GPS station data. The costs of publishing this paper have been evenly shared by SSEC and MKWC.

REFERENCES

Antonelli, P., and Coauthors, 2004: A principal component noise filter for high spectral resolution infrared measurements. *J. Geophys. Res.*, **109**, D23102, doi:10.1029/2004JD004862.

——, R. Knuteson, R. Garcia, S. Bedka, D. Tobin, J. Taylor, W. Smith, and H. Revercomb, 2008: UWPHYSRET an SSEC inversion package for high resolution infrared data based on LBLRTM. Presentation, *Fourth Annual Advanced High Spectral Resolution Infrared Observations Workshop*, Darmstadt, Germany, European Organisation for the Exploitation of Meteorological Satellites. [Available online at http://www.ssec.wisc.edu/hsr/meetings/2008/presentations/Paolo_Antonelli.pdf.]

——, T. Cherubini, T. Auligne, L. Bernardini, S. Businger, and F. Marzano, 2015: The potential of Meteosat Third Generation (MTG) Infrared Sounder (IRS) level 2 product assimilation in a very short range numerical weather forecast model. EUMETSAT Final Rep., 79 pp.

Aumann, H., and Coauthors, 2003: AIRS/AMSU/HSB on the Aqua mission: Design, science objectives, data products, and processing systems. *IEEE Trans. Geosci. Remote Sens.*, **41**, 253–264, doi:10.1109/TGRS.2002.808356.

Avriel, M., 2003: *Nonlinear Programming: Analysis and Methods.* Dover Publishing, 512 pp.

Barker, D., and Coauthors, 2012: The Weather Research and Forecasting Model's Community Variational/Ensemble Data Assimilation System: WRFDA. *Bull. Amer. Meteor. Soc.*, **93**, 831–843, doi:10.1175/BAMS-D-11-00167.1.

Blumstein, D., and Coauthors, 2004: IASI instrument: Technical overview and measured performances. *Infrared Spaceborne Remote Sensing XII*, M. Strojnik, Ed., International Society for Optical Engineering (SPIE Proceedings, Vol. 5543), 196–207.

Businger, S., R. McLaren, R. Ogasawara, D. Simons, and R. J. Wainscoat, 2002: Starcasting. *Bull. Amer. Meteor. Soc.*, **83**, 858–871, doi:10.1175/1520-0477(2002)083<0858:S>2.3.CO;2.

Cao, C., X. Xiong, A. Wu, and X. Wu, 2008: Assessing the consistency of AVHRR and MODIS L1B reflectance for generating fundamental climate data records. *J. Geophys. Res.*, **113**, D09114, doi:10.1029/2007JD009363.

——, F. De Luccia, X. Xiong, R. Wolfe, and F. Weng, 2014: Early on-orbit performance of the Visible Infrared Imaging Radiometer Suite onboard the Suomi National Polar-Orbiting Partnership (S-NPP) satellite. *IEEE Trans. Geosci. Remote Sens.*, **52**, 1142–1156, doi:10.1109/TGRS.2013.2247768.

Cao, G., T. W. Giambelluca, D. E. Stevens, and T. A. Schroeder, 2007: Inversion variability in the Hawaiian trade wind regime. *J. Climate*, **20**, 1145–1160, doi:10.1175/JCLI4033.1.

Cherubini, T., S. Businger, C. Valden, and R. Ogasawara, 2006: The impact of satellite-derived atmospheric motion vectors on mesoscale forecasts over Hawaii. *Mon. Wea. Rev.*, **134**, 2009–2020, doi:10.1175/MWR3163.1.

——, ——, and R. Lyman, 2011: An operational perspective for modeling optical turbulence. *Seeing Clearly: The Impact of Atmospheric Turbulence on the Propagation of Extraterrestrial Radiation*, S. Businger and T. Cherubini, Eds., VBW Publishing, 165–182.

Chou, S.-H., B. Zavodsky, and G. Jedlovec, 2009: Data assimilation and regional forecasts using Atmospheric Infrared Sounder (AIRS) profiles. *16th Conf. on Satellite Meteorology and Oceanography*, Phoenix, AZ, Amer. Meteor. Soc., JP6.11. [Available online at https://ams.confex.com/ams/89annual/webprogram/Paper147745.html.]

——, ——, and ——, 2010: Regional precipitation forecast with Atmospheric Infrared Sounder (AIRS) profile assimilation. *11th Annual WRF Users' Workshop*, Boulder, CO, National Center for Atmospheric Research, P.88. [Available online at http://www2.mmm.ucar.edu/wrf/users/workshops/WS2010/abstracts/P-88.pdf.]

Cooke, R., B. Wielicki, D. Young, and M. Mlynczak, 2014: Value of information for climate observing systems. *Environ. Syst. Decis.*, **34**, 98–109, doi:10.1007/s10669-013-9451-8.

Crevoisier, C., and Coauthors, 2014: Towards IASI-new generation (IASI-NG): Impact of improved spectral resolution and radiometric noise on the retrieval of thermodynamic, chemistry and climate variables. *Atmos. Meas. Tech.*, **7**, 4367–4385, doi:10.5194/amt-7-4367-2014.

De Haan, S., G.-J. Marseille, and P. de Valk, 2015: The potential of Meteosat Third Generation (MTG) Infrared Sounder (IRS) level 2 product assimilation in a very short range numerical weather forecast model. Royal Netherlands Meteorological Institute Final Rep., 90 pp.

Esposito, F., G. Grieco, G. Masiello, G. Pavese, R. Restieri, C. Serioa, and V. Cuomob, 2007: Intercomparison of line-parameter spectroscopic databases using downwelling spectral radiance. *Quart. J. Roy. Meteor. Soc.*, **133**, 191–202, doi:10.1002/qj.131.

EUMETSAT, 2014: Algorithm theoretical basis document for level 2 processing of the MTG Infra-Red Sounder data. EUMETSAT Tech. Rep., 114 pp.

Han, Y., 2015: CrIS full spectral resolution SDR and S-NPP/JPSS-1 CrIS performance status. *20th Int. TOVS Study Conf.*, Lake Geneva, WI, International TOVS Working Group, 1.07. [Available online at https://cimss.ssec.wisc.edu/itwg/itsc/itsc20/program/PDFs/28Oct/session1c/1_07_han.pdf.]

——, and Coauthors, 2013: Suomi NPP CrIS measurements, sensor data record algorithm, calibration and validation activities, and record data quality. *J. Geophys. Res. Atmos.*, **118**, 12 734–12 748, doi:10.1002/2013JD020344.

Hultberg, T., 2009: IASI principal component compression (IASI PCC) FAQ. EUMETSAT Rep., 5 pp. [Available online at http://www.eumetsat.int/website/wcm/idc/idcplg?IdcService=GET_FILE&dDocName=pdf_ipcc_faq&RevisionSelectionMethod=LatestReleased&Rendition=Web.]

Jones, T., and D. Stensrud, 2012: Assimilating AIRS temperature and mixing ratio profiles using an ensemble Kalman filter approach for convective-scale forecast. *Wea. Forecasting*, **27**, 541–563, doi:10.1175/WAF-D-11-00090.1.

Klemp, J., W. C. Skamarock, and J. Dudhia, 2007: Conservative split-explicit time integration methods for the compressible nonhydrostatic equations. *Mon. Wea. Rev.*, **135**, 2897–2913, doi:10.1175/MWR3440.1.

Levenberg, K., 1944: A method for the solution of certain nonlinear problems in least squares. *Quart. Appl. Math.*, **2**, 164–168, doi:10.1090/qam/10666.

Loveland, T., J. Merchant, D. Ohlen, and J. Brown, 1991: Development of a land-cover characteristics database for the conterminous U.S. *Photogramm. Eng. Remote Sens.*, **57**, 1453–1463.

——, Z. Zhu, D. Ohlen, J. Brown, B. Reed, and L. Yang, 1999: An analysis of the IGBP global land cover characterization process. *Photogramm. Eng. Remote Sens.*, **65**, 1069–1074.

Marquardt, D., 1963: An algorithm for least-squares estimation of nonlinear parameters. *SIAM J. Appl. Math.*, **11**, 431–441, doi:10.1137/0111030.

Masiello, G., C. Serio, and P. Antonelli, 2012: Inversion for atmospheric thermodynamical parameters of IASI data in the principal components space. *Quart. J. Roy. Meteor. Soc.*, **138**, 103–117, doi:10.1002/qj.909.

Masuda, K., T. Takashima, and Y. Takayama, 1988: Emissivity of pure and sea waters for the model sea surface in the infrared

window regions. *Remote Sens. Environ.*, **24**, 313–329, doi:10.1016/0034-4257(88)90032-6.

Migliorini, S., 2012: On the equivalence between radiance and retrieval assimilation. *Mon. Wea. Rev.*, **140**, 258–265, doi:10.1175/MWR-D-10-05047.1.

——, C. Piccolo, and C. Rodgers, 2008: Use of the information content in satellite measurements for an efficient interface to data assimilation. *Mon. Wea. Rev.*, **136**, 2633–2650, doi:10.1175/2007MWR2236.1.

Moncet, J.-L., G. Uymin, A. E. Lipton, and H. E. Snell, 2008: Infrared radiance modeling by optimal spectral sampling. *J. Atmos. Sci.*, **65**, 3917–3934, doi:10.1175/2008JAS2711.1.

Nocedal, J., and S. Wright, 1999: *Numerical Optimization.* Springer, 636 pp.

Parrish, D. F., and J. C. Derber, 1992: The National Meteorological Center's spectral statistical-interpolation analysis system. *Mon. Wea. Rev.*, **120**, 1747–1763, doi:10.1175/1520-0493(1992)120<1747:TNMCSS>2.0.CO;2.

Prates, C., S. Migliorini, L. Stewart, and J. Eyre, 2016: Assimilation of transformed retrievals obtained from clear-sky IASI measurements. *Quart. J. Roy. Meteor. Soc.*, **142**, 1697–1712, doi:10.1002/qj.2764.

Reale, O., J. Susskind, R. Rosenberg, E. Brin, E. Liu, L. P. Riishojgaard, J. Terry, and J. C. Jusem, 2008: Improving forecast skill by assimilation of quality-controlled AIRS temperature retrievals under partially cloudy conditions. *Geophys. Res. Lett.*, **35**, L08809, doi:10.1029/2007GL033002.

Rodgers, C. D., 2000: *Inverse Methods for Atmospheric Soundings: Theory and Practice*. World Scientific, 240 pp.

Serio, C., and Coauthors, 2015: Infrared Atmospheric Sounder Interferometer radiometric noise assessment from spectral residuals. *Appl. Opt.*, **54**, 5924–5936, doi:10.1364/AO.54.005924.

Singh, R., C. M. Kishtawal, S. P. Ojha, and P. K. Pal, 2012: Impact of assimilation of Atmospheric Infrared Sounder (AIRS) radiances and retrievals in the WRF 3D-Var assimilation system. *J. Geophys. Res.*, **117**, D11107, doi:10.1029/2011JD017367.

Smith, W. L., E. Weisz, S. V. Kireev, D. K. Zhou, Z. Li, and E. E. Borbas, 2012: Dual-regression retrieval algorithm for real-time processing of satellite ultraspectral radiances. *J. Appl. Meteor. Climatol.*, **51**, 1455–1476, doi:10.1175/JAMC-D-11-0173.1.

Strow, L. L., and Coauthors, 2013: Spectral calibration and validation of the Cross-track Infrared Sounder on the Suomi NPP satellite. *J. Geophys. Res. Atmos.*, **118**, 12 486–12 496, doi:10.1002/2013JD020480.

Tobin, D., and Coauthors, 2006: Atmospheric Radiation Measurement site atmospheric state best estimates for Atmospheric Infrared Sounder temperature and water vapor retrieval validation. *J. Geophys. Res.*, **111**, D09S14, doi:10.1029/2005JD006103.

——, and Coauthors, 2013: Suomi-NPP CrIS radiometric calibration uncertainty. *J. Geophys. Res. Atmos.*, **118**, 10 589–10 600, doi:10.1002/jgrd.50809.

Zhou, D. K., A. Larar, X. Liu, W. L. Smith, L. L. Strow, P. Yang, P. Schlüssel, and X. Calbet, 2011: Global land surface emissivity retrieved from satellite ultraspectral IR measurements. *IEEE Trans. Geosci. Remote Sens.*, **49**, 1277–1290, doi:10.1109/TGRS.2010.2051036.

Zhu, Y., and R. E. Newell, 1994: Atmospheric rivers and bombs. *Geophys. Res. Lett.*, **21**, 1999–2002, doi:10.1029/94GL01710.